Electromagnetic Performance Prediction for the Symmetrical Dual Three-phase Surface-mounted PMSM under Open-phase Faults Based on Accurate Subdomain Model

Zhe Liang, *Member*, *IEEE*, Deliang Liang, *Senior Member*, *IEEE*, Peng Kou, *Senior Member*, *IEEE* and Shaofeng Jia, *Member*, *IEEE*

***Abstract*—The paper presents an accurate analytical subdomain model for predicting the electromagnetic performance in the symmetrical dual three-phase surface-mounted permanent magnet synchronous machine (PMSM) under open-phase faulty conditions. The model derivations are extended from previous accurate subdomain models accounting for slotting effects. Compared with most conventional subdomain models for traditional three-phase machines with nonoverlapping winding arrangement, the subdomain model proposed in this paper applied for the 24-slot/4-pole dual three-phase machine with symmetrical overlapping winding arrangement. In order to investigate the postfault electromagnetic performance, the reconfigured phase currents and then current density distribution in stator slots under different open-circuit conditions are discussed. According to the developed model and postfault current density distribution, the steady-state electromagnetic performance, such as the electromagnetic torque and unbalanced magnetic force, under open-circuit faulty conditions are obtained. For validation purposes, finite element analysis (FEA) is employed to validate the analytical results. The result indicate that the postfault electromagnet performance can be accurately predicted by the proposed subdomain model, which is in good agreement with FEA results.**

***Index Terms*—Dual three-phase, Permanent magnet synchronous machine, Subdomain model, Electromagnetic torque, Unbalanced magnetic force, Open-phase fault.**

I. Introduction

DUAL three-phase machines, or six-phase machines, as one of most popular multiphase machines, have received increased attention in last decades [1], [2]. Dual three-phase permanent magnet (PM) machines combine the advantages of high efficiency and torque density due to the use of PM materials. Owing to their inherent fault-tolerant capability, dual three-phase machines are always used in high-reliability-required applications where the uninterrupted service is demanded, such as aircrafts, electric vehicles, ship propulsion and some industrial fields. The existence of redundant phases provides the opportunity of continuous operation when one or several phases are open-circuit. In order to improve the fault-tolerant capability of the dual three-phase drives in event of open-circuit faults, fault-tolerant control strategies involving hardware reconfiguration and remaining healthy phase currents readaptation are always required. Consequently, several recent research has focused on the postfault control strategies and postfault electromagnetic performance prediction for dual three-phase machines under open-circuit faulty condition[3-6].

Postfault control for dual three-phase machines with one or several phases open-circuit have been intensively investigated in past research studies[7-10]. The control strategies for postfault current readaptation can be classified into two categories: 1) Hysteresis current control to maintain the unchanged rotating magnetomotive force (MMF)[7]; 2) Field oriented control with the postfault reduced-order dynamic model[8, 9]; 3) predictive model control[10]. Nevertheless, these control methods are based on the lumped-parameter models including voltage, flux and torque equations. The detailed performance such as the cogging torque ripples, unbalanced magnetic force due to the asymmetrical operation under faulty conditions cannot be presented. Therefore, an accurate model involving the machine topology are required for further analysis on the postfault electromagnetic performance of the dual three-phase machines under open-phase faulty conditions.

To evaluate the postfault electromagnetic performance with a certain machine geometry, numerical approaches such as finite element analysis (FEA) is a powerful tool because of their high accuracy and capability of nonlinear problem. However, the FEA method is time-consuming and hard to provide a close-form expression between the performance and parameters. Furthermore, several electromagnetic characteristics calculations, as cogging torque and force calculations, are sensitive to FE geometric meshes. To overcome the drawbacks brought by FEA approaches, analytical methods can provide

Manuscript received January 30, 2022; revised March 20, 2022; accepted May 09, 2022. date of publication December 25, 2022; date of current version December 18, 2022.

This work was supported in part by National Natural Science Foundation of China (NSFC) under Project No. 51737010, and in part by State Key Laboratory of Electrical Insulation and Power Equipment (EIPE19109).

Zhe Liang, Deliang Liang, Peng Kou, and Shaofeng Jia are with the Xi'an Jiaotong University, Xi'an, 710049, China.(e-mail: liangzhe@stu.xjtu.edu.cn; dlliang@mail.xjtu.edu.cn; koupeng@mail.xjtu.edu.cn; shaofengjia@mail.xjtu.edu.cn)

(Corresponding Author: Deliang Liang)

Digital Object Identifier 10.30941/CESTEMS.2022.00054

enough accurate solutions with relatively shorter computational time in comparison with FEA approaches. In addition, their calculations avoid meshing so can obtain mesh-independent results.

Analytical model applied for magnetic field distribution and electromagnetic performance prediction can be traced back to a long time ago. Many comprehensive reviews about the analytical approaches have been published in [11-13]. In order to accurately predict the postfault electromagnetic torque and unbalanced magnetic force, slotting effect must be taken into account in the analytical model. The analytical models considering slotting effects can be divided into two categories: 1) Conformal transformation with Carter's factor[14], relative permeance model[15] or complex relative permeance model[16], which maps the slotted regions into slotless ones; 2) Subdomain model. The main idea of this method is directly solving Maxwell's equations in all subdomains (Laplace's equations in air-gap and slot-opening regions, Possion's equations in PM and slot regions) by the separation of variables technique. The Fourier coefficients of all subdomain solutions can be determined by the boundary conditions on the interfaces between the subdomains. In previous literature[12-20], subdomain methods have been successfully applied into PM machines with different rotor types including 1) surface-mounted [13, 17], 2) inset[18, 19], and 3) spoke-type[20]; 4) with various pole and slot combination[12]; 5) with different magnetization patterns including parallel and radial magnetizations[21]. The magnet field distribution under open-circuit, armature reaction and on-load conditions have been sufficiently investigated using subdomain models. Furthermore, the cogging torque, back electromotive force (EMF) under the open-circuit condition and electromagnetic torque, unbalanced magnetic force under on-load conditions have also been predicted.

In past investigations, the analytical subdomain models have been proved an effective way to predict magnetic field distribution and electromagnetic performance. Although different kinds of subdomain models have been developed to deal with different machine geometries and topologies, there still exist some gaps to fill: 1) Although subdomain models for PM machines with overlapping windings have been developed in [17], models for dual three-phase PM machines with symmetrical overlapping winding arrangement have not been proposed by previously published reports. 2) Postfault electromagnetic performance, for instance, electromagnetic torque and unbalanced magnetic force, under asymmetrical faulty operation situation have not been analyzed by previous works.

To fill the above-mentioned gaps, we developed the accurate subdomain model for the 24-slot/4-pole symmetrical dual three-phase PM machine. The analytical subdomain model is established with symmetrical overlapping double-layer windings. The vector magnetic potential of all subdomains are calculated by using variable separation technique with appropriate boundary and interface conditions. The current density distribution in stator slots also influence the magnetic field distribution and further influence the electromagnetic performance. Therefore, all possible operating modes for the symmetrical dual three-phase machine under different open-phase conditions have been investigated. The corresponding steady-steady phase currents are obtained by reserving the postfault *d*- and *q*-component of currents with proper coordinate transformations. Based on the developed subdomain model, the postfault electromagnetic torque, torque ripples and unbalanced magnetic force are predicted. Finally, the accuracy of the proposed model and derived electromagnetic performance are validated using FEA method.

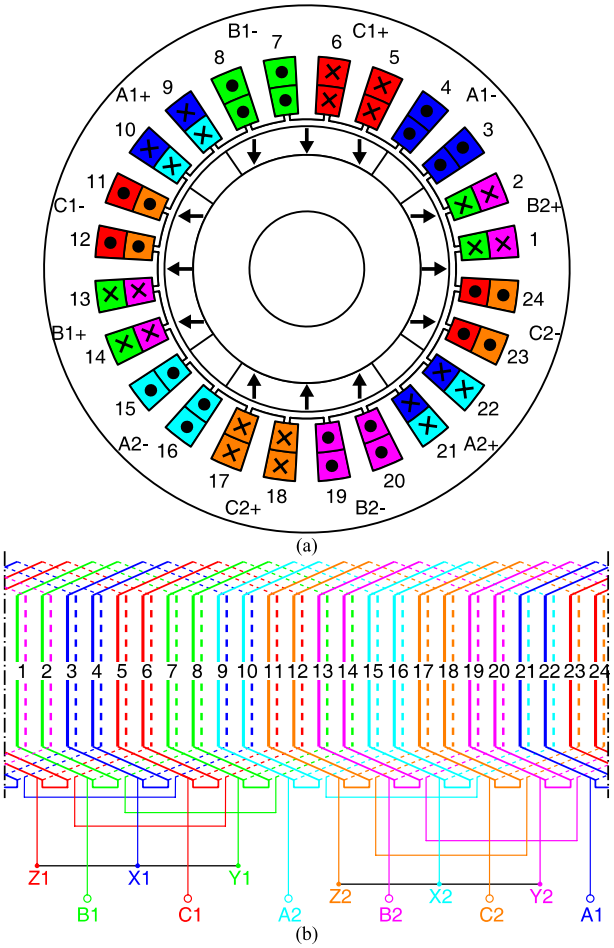

Fig. 1. Geometry of a 24-slot/4-pole dual three-phase surface-mounted PM machine with symmetrical winding configuration. (a) Geometry structure. (b) Winding configuration. Solid lines represent the conductors in upper-layer slots and dotted line represent the conductors in lower-layer slots.

The rest of this paper is organized as follows. The machine geometry and winding arrangement are demonstrated in Section II. Section III establishes the analytical subdomain model and derives the general solutions. Section IV discusses the fault-tolerant operating modes and the corresponding current distribution in stator slots. In Section V, analytical predicted formulae for global electromagnetic quantities, such as back-EMF, electromagnetic torque and unbalanced magnetic force are presented. Section VI shows the analytical results compared and validated with the FEA results. Finally, Section VII summarizes the conclusions of this paper.

II. Machine Geometry and Winding Configuration

The geometric structure of the 24-slot/4-pole symmetrical

TABLE I
MAIN PARAMETERS OF THE SYMMETRICAL DUAL THREE-PHASE PMSM

Parameters	Value
Slot number, N_s	24
Pole-pair number, p	2
Stator outer diameter, $2R_s$	91.5 mm
Stator inner diameter, $2R_3$	52 mm
Rotor outer diameter, $2R_2$	49.6 mm
Magnet inner diameter, $2R_1$	39.6 mm
Rotor inner diameter, $2R_r$	20 mm
Magnet thickness, h_m	10 mm
Airgap length, l_g	1.2 mm
Slot-opening angle, β	2° (mech.)
Winding slot angle, γ	8° (mech.)
Stator yoke height, h_y	8.85 mm
Slot layer pattern	Double-layer
Winding turns, N_t	11
Active length, L	82 mm
Magnetization pattern	Parallel
Remanence, B_r	0.96 T
Pole-arc coefficient, α_P	0.77
Relative recoil permeability, μ_r	1.06
Rated speed	3000 rpm
Rated torque	3.2 Nm
Rated cureent (A_{RMS})	5.3 A
Maximum harmonic order for Region *I*/*II*, *K*	100
Maximum harmonic order for Region *IIIi*, *M*	10
Maximum harmonic order for Region *IVi*/*Vi*, *N*	40

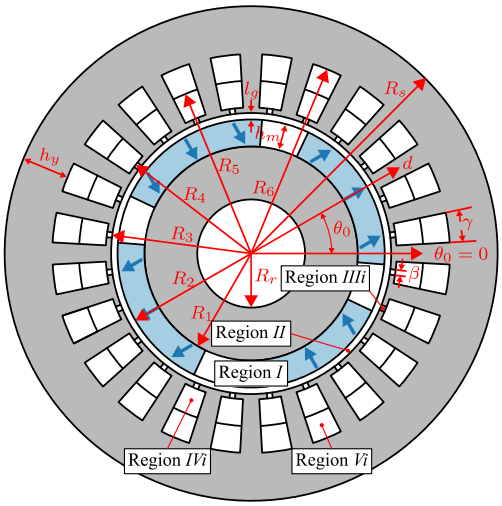

Fig. 2. Symbols and five regions (Region *I*: PMs, Region *II*: airgap, Region *IIIi*: the *i*th slot-opeing, Region *IVi*: the *i*th upper layer slot, Region *Vi*: the *i*th lower layer slot).

dual three-phase surface-mounted PM machine with symmetrical overlapping windings and semi-closed slots is shown in Fig. 1(a). The machine geometry accounts for stator slotting effects. The machine parameters are given in Table I. The geometric parameters are defined as the stator outer radius R_s, the stator inner radius R_3, the rotor outer radius R_2, the magnet inner radius R_1, the rotor inner radius R_r, the magnet thickness h_m, the air-gap thickness l_g, the stator yoke height h_y, the slot-opening angle β and the slot angle γ. This machine type has two completely symmetrical sets of three-phase windings, which are spatially embedded in the double-layer slots of the completely separated parts of the stator without electrical degree shifted. The symmetrical winding arrangement results in the symmetrical MMFs and back-EMFs of two three-phase windings. Each phase winding has four coils. The two three-phase windings are labeled as A1B1C1 and A2B2C2, respectively. They are Y-connected and have independent neutrals. The winding arrangement shown in Fig. 1(b).

III. ANALYTICAL FIELD MODEL AND SOLUTIONS

A. Subdomain Model

In order to simplify the model, the proposed model is expressed by the vector magnet potential in 2-D polar coordinates with the following assumptions: 1) the magnetic permeability of the stator and rotor iron cores is infinite; 2) eddy current effects and end effects are neglected; 3) the magnetic circuit is linear; 4) The relative recoil permeability of magnets is constant but not unity; 5) the rotor PMs, stator slot-openings and slots have only radial and tangential sides; 6) stator/rotor laminations are nonconductive; 7) uniform current density in the area of the coil; and 8) the vector magnetic potential has only z-component, and only depends on r and θ, in 2-D polar coordinate.

As shown in Fig. 2, the magnetic field domain can be divided into five subdomains: the rotor PM subdomain (Region *I*), the air-gap subdomain (Region *II*), the i th slots-opening subdomains (Region *IIIi*, $i = 1,2,\ldots,N_s$.), the ith slot upper layer subdomain (Region *IVi*) and lower layer subdomain (Region *Vi*). The geometrical parameters of all subdomains are shown in Fig. 2.

The general expressions of the potential distributions in 2-D polar coordinates are given by (1)–(5). The equations in the PMs and slots subdomains are Poisson's equations and the equations in the slot-opening and air-gap subdomains are Laplace's equations:

$$\frac{\partial^2 A_I}{\partial r^2}+\frac{1}{r}\frac{\partial A_I}{\partial r}+\frac{1}{r^2}\frac{\partial^2 A_I}{\partial \theta^2}=-\frac{\mu_0}{r}\left(M_\theta-\frac{\partial M_r}{\partial \theta}\right),(r,\theta)\in\mathcal{D}_I \quad (1)$$

$$\frac{\partial^2 A_{II}}{\partial r^2}+\frac{1}{r}\frac{\partial A_{II}}{\partial r}+\frac{1}{r^2}\frac{\partial^2 A_{II}}{\partial \theta^2}=0,(r,\theta)\in\mathcal{D}_{II} \quad (2)$$

$$\frac{\partial^2 A_{IIIi}}{\partial r^2}+\frac{1}{r}\frac{\partial A_{IIIi}}{\partial r}+\frac{1}{r^2}\frac{\partial^2 A_{IIIi}}{\partial \theta^2}=0,(r,\theta)\in\mathcal{D}_{IIIi} \quad (3)$$

$$\frac{\partial^2 A_{IVi}}{\partial r^2}+\frac{1}{r}\frac{\partial A_{IVi}}{\partial r}+\frac{1}{r^2}\frac{\partial^2 A_{IVi}}{\partial \theta^2}=-\mu_0 J_{Ui},(r,\theta)\in\mathcal{D}_{IVi} \quad (4)$$

$$\frac{\partial^2 A_{Vi}}{\partial r^2}+\frac{1}{r}\frac{\partial A_{Vi}}{\partial r}+\frac{1}{r^2}\frac{\partial^2 A_{Vi}}{\partial \theta^2}=-\mu_0 J_{Li},(r,\theta)\in\mathcal{D}_{Vi} \quad (5)$$

where $\mathcal{D}_I=\{(r,\theta)\,|\,R_1\le r\le R_2, 0\le\theta\le 2\pi\}$,

$\mathcal{D}_{II}=\{(r,\theta)\,|\,R_2\le r\le R_3, 0\le\theta\le 2\pi\}$,

$\mathcal{D}_{IIIi}=\{(r,\theta)\,|\,R_3\le r\le R_4, \theta_i-\beta/2\le\theta\le\theta_i+\beta/2\}$,

$\mathcal{D}_{IVi}=\{(r,\theta)\,|\,R_4\le r\le R_5, \theta_i-\gamma/2\le\theta\le\theta_i+\gamma/2\}$,

$\mathcal{D}_{Vi}=\{(r,\theta)\,|\,R_5\le r\le R_6, \theta_i-\gamma/2\le\theta\le\theta_i+\gamma/2\}$; θ_i is the ith slot position angle; μ_0 is the permeability of the vacuum, M_r and M_θ are the radial and tangential magnetization of PMs, relatively.

The magnetization of magnets with either radial or parallel magnetization methods has been derived in [21], for parallel magnetization used in this paper, the magnetization of magnets

can be expressed as Fourier series form, i.e.,

$$M_r = \sum_{\frac{k}{p}=1,3,\cdots}^{\infty} M_{rk}\cos k(\theta-\theta_0) = \sum_{\frac{k}{p}=1,3,\cdots}^{\infty} \left(M_{rck}\cos k\theta + M_{rsk}\sin k\theta\right) \tag{6}$$

$$M_\theta = \sum_{\frac{k}{p}=1,3,\cdots}^{\infty} M_{\theta k}\sin k(\theta-\theta_0) = \sum_{\frac{k}{p}=1,3,\cdots}^{\infty} \left(M_{\theta ck}\cos k\theta + M_{\theta sk}\sin k\theta\right) \tag{7}$$

where $M_{rck} = M_{rk}\cos k\theta_0$, $M_{rsk} = M_{rk}\sin k\theta_0$, $M_{\theta ck} = -M_{\theta k}\sin k\theta_0$, $M_{\theta sk} = M_{\theta k}\cos k\theta_0$; θ_0 is the rotor position angle.

when $k \neq 1$ and $p \neq 1$, M_{rk} and $M_{\theta k}$ can be expressed as

$$M_{rk} = \frac{B_r\alpha_P}{\mu_0}\left(\frac{\sin(k+1)\frac{\alpha_P\pi}{2p}}{(k+1)\frac{\alpha_P\pi}{2p}} + \frac{\sin(k-1)\frac{\alpha_P\pi}{2p}}{(k-1)\frac{\alpha_P\pi}{2p}}\right) \tag{8}$$

$$M_{\theta k} = \frac{B_r\alpha_P}{\mu_0}\left(\frac{\sin(k+1)\frac{\alpha_P\pi}{2p}}{(k+1)\frac{\alpha_P\pi}{2p}} - \frac{\sin(k-1)\frac{\alpha_P\pi}{2p}}{(k-1)\frac{\alpha_P\pi}{2p}}\right) \tag{9}$$

where B_r is the remanence, α_P is the pole-arc coefficient, μ_0 is the vacuum permeability.

In (1)–(5), J_{Ui} and J_{Li} are both constants representing the current density of the upper and the lower layers of the *i*th slot, respectively. In this 6-phase/24-slot machine, the distribution of J_{Ui} and J_{Li} can be expressed as

$$\mathrm{row}(J_{Ui})_i = \tfrac{1}{A_U}\mathrm{row}(I_j)_j \cdot \mathbf{C}_U, \tag{10}$$

$$\mathrm{row}(J_{Li})_i = \tfrac{1}{A_L}\mathrm{row}(I_j)_j \cdot \mathbf{C}_L \tag{11}$$

where $\mathrm{row}(\cdot)_i$, $\mathrm{row}(\cdot)_j$ means the row vector spanned by the "·" elements with the subscript *i* and *j*, respectively ($i = 1,2,\ldots,N_s$, $j = 1,2,\ldots m$; A_U and A_L are the corresponding cross section areas of upper- and lower-layer coils, i.e., $A_U = \frac{1}{2}\gamma\left(R_5^2 - R_4^2\right)$ and $A_L = \frac{1}{2}\gamma\left(R_6^2 - R_5^2\right)$; $\mathbf{C}_U$ and $\mathbf{C}_L$ are the connection matrix (with the dimension $m \times N_s$, m is the phase number and N_s is the slot number) that presents the stator windings distribution in the slot upper- and lower-layers, respectively. The element $C_{ij} = 1$ of $\mathbf{C}_U$ and $\mathbf{C}_L$ means the coils in slot-j is belong to the phase-*i* and the direction is positive; $C_{ij} = -1$ means the coils in slot-*j* is belong to the phase-*i* and the direction is negative; $C_{ij} = 0$ means the coils in slot-j and the phase-i have no connection. According to Fig. 1, $\mathbf{C}_U$ and $\mathbf{C}_L$ in this 4-pole/24-slot dual three-phase machine type can be expressed as: 1) 1st row (phase-*a*1): $\mathbf{C}_U(3,4) = -1$, $\mathbf{C}_U(21,22) = 1$, $\mathbf{C}_L(3,4) = -1$, $\mathbf{C}_L(9,10) = 1$; 2) 2nd row (phase-*b*1): $\mathbf{C}_U(1,2) = 1$, $\mathbf{C}_U(7,8) = -1$, $\mathbf{C}_L(7,8) = -1$, $\mathbf{C}_L(13,14) = 1$; 3) 3rd row (phase-*c*1): $\mathbf{C}_U(5,6) = 1$, $\mathbf{C}_U(23,24) = -1$, $\mathbf{C}_L(5,6) = 1$, $\mathbf{C}_L(11,12) = -1$; 4) 4th row (phase-*a*2): $\mathbf{C}_U(9,10) = 1$, $\mathbf{C}_U(15,16) = -1$, $\mathbf{C}_L(15,16) = -1$, $\mathbf{C}_L(21,22) = 1$; 5) 5th row (phase-*b*2): $\mathbf{C}_U(13,14) = 1$, $\mathbf{C}_U(19,20) = -1$, $\mathbf{C}_L(1,2) = 1$, $\mathbf{C}_L(19,20) = -1$; 6) 6th row (phase-*c*2): $\mathbf{C}_U(11,12) = -1$, $\mathbf{C}_U(17,18) = 1$, $\mathbf{C}_L(17,18) = 1$, $\mathbf{C}_L(23,24) = -1$.

By using the separation of variables technique, the general solutions of (1)–(5) with the homogeneous boundary conditions (12)–(16) are given in (17)–(21).

$$H_{I\theta}(R_1,\theta) = 0,$$

$$\text{or } \left(-\frac{1}{\mu_0\mu_r}\frac{\partial A_I}{\partial r} - \frac{1}{\mu_r}M_\theta\right)\Big|_{r=R_1} = 0, \quad \forall\theta \in (0,2\pi) \tag{12}$$

$$H_{IIIi\theta}(r,\theta_i - \frac{\beta}{2}) = H_{IIIi\theta}(r,\theta_i + \frac{\beta}{2}) = 0,$$

$$\text{or } \frac{\partial A_{IIIi}}{\partial\theta}\Big|_{\theta=\theta_i-\frac{\beta}{2}} = \frac{\partial A_{IIIi}}{\partial\theta}\Big|_{\theta=\theta_i+\frac{\beta}{2}} = 0, \quad \forall r \in (R_3,R_4) \tag{13}$$

$$H_{IVi\theta}(r,\theta_i - \frac{\gamma}{2}) = H_{IVi\theta}(r,\theta_i + \frac{\gamma}{2}) = 0,$$

$$\text{or } \frac{\partial A_{IVi}}{\partial\theta}\Big|_{\theta=\theta_i-\frac{\gamma}{2}} = \frac{\partial A_{IVi}}{\partial\theta}\Big|_{\theta=\theta_i+\frac{\gamma}{2}} = 0, \quad \forall r \in (R_4,R_5) \tag{14}$$

$$H_{Vi\theta}(r,\theta_i - \frac{\gamma}{2}) = H_{Vi\theta}(r,\theta_i + \frac{\gamma}{2}) = 0,$$

$$\text{or } \frac{\partial A_{Vi}}{\partial\theta}\Big|_{\theta=\theta_i-\frac{\gamma}{2}} = \frac{\partial A_{Vi}}{\partial\theta}\Big|_{\theta=\theta_i+\frac{\gamma}{2}} = 0, \quad \forall r \in (R_5,R_6) \tag{15}$$

$$H_{Vi\theta}(R_6,\theta) = 0,$$

$$\text{or } \frac{\partial A_{Vi}}{\partial r}\Big|_{r=R_6} = 0, \quad \forall\theta \in (\theta_i - \frac{\gamma}{2},\theta_i + \frac{\gamma}{2}) \tag{16}$$

The general solution of (1)–(5) can be given by

$$\begin{aligned} A_I(r,\theta) &= \sum_{k=1}^{\infty} A_{Ik}G_{1k}(r)\cos k\theta + C_{Ik}G_{1k}(r)\sin k\theta \\ &+ \sum_{\frac{k}{p}=1,3,\cdots}^{\infty} \frac{\mu_0}{k^2-1}\Big[\left(G_{2k}(r)M_{\theta ck} - G_{2k}(r)M_{rsk}\right)\cos k\theta \\ &+ \left(G_{2k}(r)M_{\theta sk} + G_{3k}(r)M_{rck}\right)\sin k\theta\Big] \end{aligned} \tag{17}$$

where

$$G_{1k}(r) = \left(\frac{r}{R_1}\right)^k + \left(\frac{R_1}{r}\right)^k,$$

$$G_{2k}(r) = r + kR_1\left(\frac{R_1}{r}\right)^k,$$

$$G_{3k}(r) = kr + R_1\left(\frac{R_1}{r}\right)^k.$$

$$\begin{aligned} A_{II}(r,\theta) &= \sum_{k=1}^{\infty}\left(A_{IIk}\left(\frac{r}{R_2}\right)^k + B_{IIk}\left(\frac{R_3}{r}\right)^k\right)\cos k\theta \\ &+ \sum_{k=1}^{\infty}\left(C_{IIk}\left(\frac{r}{R_2}\right)^k + D_{IIk}\left(\frac{R_3}{r}\right)^k\right)\sin k\theta \end{aligned} \tag{18}$$

$$A_{IIIi}(r,\theta)=A_{IIIi,0}+B_{IIIi,0}\ln r+\sum_{m=1}^{\infty}\left(A_{IIIi,m}\left(\frac{r}{R_3}\right)^{v_m}+B_{IIIi,m}\left(\frac{R_4}{r}\right)^{v_m}\right)\cos v_m\left(\theta-\theta_i+\frac{\beta}{2}\right) \quad (19)$$

$$A_{IVi}(r,\theta)=A_{IVi,0}+B_{IVi,0}\ln r-\frac{1}{4}\mu_0 J_{Ui}r^2+\sum_{n=1}^{\infty}\left(A_{IVi,n}\left(\frac{r}{R_4}\right)^{\omega_n}+B_{IVi,n}\left(\frac{R_5}{r}\right)^{\omega_n}\right)\cos\omega_n\left(\theta-\theta_i+\frac{\gamma}{2}\right) \quad (20)$$

$$A_{Vi}(r,\theta)=A_{Vi,0}+\frac{1}{2}\mu_0 J_{Li}R_6^2\ln r-\frac{1}{4}\mu_0 J_{Li}r^2+\sum_{n=1}^{\infty}A_{Vi,n}\left(\left(\frac{r}{R_5}\right)^{\omega_n}+\left(\frac{R_6}{R_5}\right)^{\omega_n}\left(\frac{R_6}{r}\right)^{\omega_n}\right)\cos\omega_n\left(\theta-\theta_i+\frac{\gamma}{2}\right) \quad (21)$$

where A_{Ik}, C_{Ik}, A_{IIk}, B_{IIk}, C_{IIk}, D_{IIk}, $A_{IIIi,m}$, $B_{IIIi,m}$, $A_{IVi,n}$, $B_{IVi,n}$ and $A_{Vi,n}$ are the harmonic coefficients to be determined by the interface conditions; $v_m=m\pi/\beta$ and $\omega_n=n\pi/\gamma$.

Based on the general field solutions (17)–(21), the radial and tangential components of the flux density of all subdomains can be derived from the vector magnetic potential by

$$B_r=\frac{1}{r}\frac{\partial A}{\partial\theta}\ \text{and}\ B_\theta=-\frac{\partial A}{\partial r}. \quad (22)$$

where B_r and B_θ are the radial and tangential components of the flux density, respectively.

B. Determination of the Boundary Conditions and the Integration Coefficient

In each subdomain region, the harmonic coefficients can be determined according to the interface conditions. The continuity of the radial flux density B_r and the tangential field strength H_θ are used to derive these conditions. These conditions can be expressed with magnetic potential vector as follows:

1) Interface Conditions between PMs (Region I) and Air Gap (Region II):

$$A_I(R_2,\theta)=A_{II}(R_2,\theta),\quad \forall\theta\in(0,2\pi) \quad (23)$$

$$\frac{1}{\mu_r}\frac{\partial A_I}{\partial r}\bigg|_{r=R_2}+\frac{\mu_0}{\mu_r}M_\theta=\frac{\partial A_{II}}{\partial r}\bigg|_{r=R_2},\quad \forall\theta\in(0,2\pi) \quad (24)$$

2) Interface Conditions between Air Gap (Region II) and ith Slot Opening (Region IIIi):

$$A_{II}(R_3,\theta)=A_{IIIi}(R_3,\theta),\quad \forall\theta\in(\theta_i-\frac{\beta}{2},\theta_i+\frac{\beta}{2}) \quad (25)$$

$$\frac{\partial A_{II}}{\partial r}\bigg|_{r=R_3}=\begin{cases}\dfrac{\partial A_{IIIi}}{\partial r}\bigg|_{r=R_3}, & \forall\theta\in(\theta_i-\dfrac{\beta}{2},\theta_i+\dfrac{\beta}{2}),\\ 0, & \text{otherwise.}\end{cases} \quad (26)$$

3) Interface Conditions between ith Slot Opening (Region IIIi) and ith Slot Upper Layer (Region IVi):

$$A_{IVi}(R_4,\theta)=A_{IIIi}(R_4,\theta),\quad \forall\theta\in(\theta_i-\frac{\beta}{2},\theta_i+\frac{\beta}{2}) \quad (27)$$

$$\frac{\partial A_{IVi}}{\partial r}\bigg|_{r=R_3}=\begin{cases}\dfrac{\partial A_{IIIi}}{\partial r}\bigg|_{r=R_3}, & \forall\theta\in(\theta_i-\dfrac{\beta}{2},\theta_i+\dfrac{\beta}{2}),\\ 0, & \forall\theta\in(\theta_i-\dfrac{\gamma}{2},\theta_i-\dfrac{\beta}{2})\cup(\theta_i+\dfrac{\beta}{2},\theta_i+\dfrac{\gamma}{2})\end{cases} \quad (28)$$

4) Interface Conditions between ith Upper Layer (Region IVi) and ith Lower Layer (Region Vi):

$$A_{IVi}(R_5,\theta)=A_{Vi}(R_5,\theta),\ \forall\theta\in(\theta_i-\frac{\gamma}{2},\theta_i+\frac{\gamma}{2}) \quad (29)$$

$$\frac{\partial A_{IVi}}{\partial r}\bigg|_{r=R_5}=\frac{\partial A_{Vi}}{\partial r}\bigg|_{r=R_5},\ \forall\theta\in(\theta_i-\frac{\gamma}{2},\theta_i+\frac{\gamma}{2}) \quad (30)$$

By applying these interface conditions, the unknown harmonic coefficients (from A_{Ik} to $A_{Vi,n}$) listed in previous subsection can be calculated. The detailed derivation process is shown in the Appendix.

According to the above analysis, the whole magnetic field general solutions of five subdomains can be completely determined by (17)–(21). The harmonic coefficients can be determined by (23)–(30). According to the governing equations (1)–(5), besides PMs, the current density distribution J_{Ui} and J_{Li} in the stator slots also act on the magnetic field distribution as armature reaction, and hence effect electromagnetic performance. The next section will discuss all possible operating modes and their corresponding steady-state currents including normal operation and fault-tolerant operation in this symmetrical dual three-phase machine type.

IV. Fault-Tolerant Operating Modes

The symmetrical dual three-phase PMSM studied in this paper can be operated with one or several phases open-circuit by using proper fault-tolerant control strategies. The aim of the fault-tolerant control is to maintain the postfault torque as much as possible by readapting remaining phase currents. The torque can be preserved if the postfault fundamental MMF/back EMF is kept as in prefault condition.

The key issue in fault-tolerant operation is to determine the remaining healthy phase currents against the situations of different open-phase faults. The symmetrical dual three-phase machine with independent neutral points can be regarded as two individual three-phase machines sharing the same rotor. Each three-phase winding can be operated as three-phase mode (T mode) or two-phase mode (D mode). In T mode, symmetrical three-phase currents flow thought the three-phase windings. Applying the traditional orthogonal Park transformation, the steady-state phase currents in T mode can be expressed as

$$I_a=\sqrt{\tfrac{2}{3}}\left(I_d\cos\theta-I_q\sin\theta\right) \quad (31)$$

$$I_b=\sqrt{\tfrac{2}{3}}\left(I_d\cos\left(\theta-\tfrac{2\pi}{3}\right)-I_q\sin\left(\theta-\tfrac{2\pi}{3}\right)\right) \quad (32)$$

$$I_c=\sqrt{\tfrac{2}{3}}\left(I_d\cos\left(\theta+\tfrac{2\pi}{3}\right)-I_q\sin\left(\theta+\tfrac{2\pi}{3}\right)\right) \quad (33)$$

where I_a, I_b and I_c are the phase-a, phase-b and phase-c currents, respectively; I_d and I_q are the d- and q-axis currents in the synchronous rotating frame, respectively; θ is the rotor electrical angle.

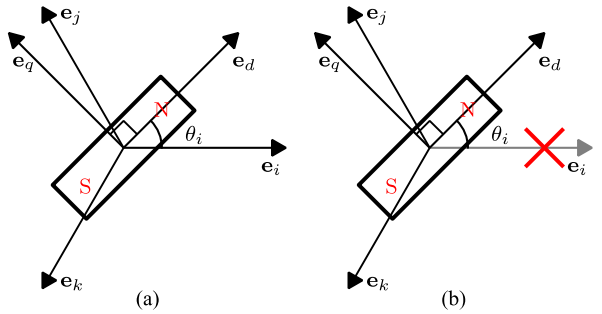

Fig. 3.Relationship between the three-phase base vectors in *abc* frame and those in *dq* frame. (a) T mode. (b) D mode. *ijk* can be *abc*, *bca* and *cab*.

When one of the two three-phase windings is operated in D mode, one-phase faulty winding is completely cut off. Asymmetrical phase currents flow though the remaining two-phase windings. In order to maintain the fundamental MMF/back EMF in D mode as the same as those in T mode. A reduced-order transformation is required to obtain the relationship between the phase currents in *abc* frame and those currents in *dq* frame.

The reduce-order current transformation can be derived from base vector transformation. The base vector transformation is used to mapping the base vectors in *abc* frame into *dq* frame. Fig .3 depicts the relationship between the base vectors in *abc* frame and those in *dq* frame under T mode and D mode. From Fig. 3, the base vector transformation in D mode can be represented by the matrix $\mathbf{E}_{jk}$ expressed as follows,

$$\mathbf{E}_{jk}=\begin{bmatrix}\mathbf{e}_j & \mathbf{e}_k\end{bmatrix}=\begin{bmatrix}\cos(\theta_i-\frac{2\pi}{3}) & \cos(\theta_i+\frac{2\pi}{3})\\ -\sin(\theta_i-\frac{2\pi}{3}) & -\sin(\theta_i+\frac{2\pi}{3})\end{bmatrix} \tag{34}$$

By using the singular value decomposition technique, $\mathbf{E}_{jk}$ can be decomposed as

$$\mathbf{E}_{jk}=\mathbf{R}(\theta_i)\mathbf{D}\mathbf{Q}^{\top} \tag{35}$$

where

$$\mathbf{R}(\theta_i)=\begin{bmatrix}\cos\theta_i & \sin\theta_i\\ -\sin\theta_i & \cos\theta_i\end{bmatrix},\mathbf{D}=\begin{bmatrix}\sqrt{3} & 0\\ 0 & 1\end{bmatrix},\mathbf{Q}^{\top}=\sqrt{\frac{1}{2}}\begin{bmatrix}-1 & 1\\ -1 & -1\end{bmatrix}^{\top}.$$

According to the relationship between base vector transformation and coordinate transformation, the current transformation and its inverse transformation mapping current vectors from *abc* frame to *dq* frame can be expressed as

$$\mathbf{T}_{jk}=(\mathbf{E}_{jk}^{\top})^{-1}=\mathbf{R}(\theta_i)\mathbf{D}^{-1}\mathbf{Q}^{\top} \tag{36}$$

$$\mathbf{T}_{jk}^{-1}=\mathbf{E}_{jk}^{\top}=\mathbf{Q}\mathbf{D}\mathbf{R}^{\top}(\theta_i) \tag{37}$$

By using the transformation in (37), the phase currents in D mode can be uniformly expressed as

$$I_i=0, \tag{38}$$

$$I_j=\sqrt{2}\left(I_d\cos\left(\theta_i-\frac{5\pi}{3}\right)-I_q\sin\left(\theta_i-\frac{5\pi}{3}\right)\right) \tag{39}$$

$$I_k=\sqrt{2}\left(I_d\cos\left(\theta_i+\frac{5\pi}{3}\right)-I_q\sin\left(\theta_i+\frac{5\pi}{3}\right)\right) \tag{40}$$

where I_i, I_j and I_k are the three-phase winding currents; *ijk* are the positive-sequence index, as *abc*, *bca* and *cab*; Phase-*i* is the open-circuit phase, phase-*b* and phase-*c* are the remaining healthy phases; $\theta_i=\theta+\phi_i$, $\phi_i=\left\{0,-\frac{2\pi}{3},\frac{2\pi}{3}\right\}$ for $ijk=\{abc,bca,cab\}$.

Summing (38), (39) and (40), the neutral point current in D mode can be expressed

$$I_n=I_i+I_j+I_k=\sqrt{6}\left(I_d\cos\theta_i-I_q\sin\theta_i\right) \tag{41}$$

As seen in (41), the neutral point current is nonzero, which means that an extra hardware in practice is demanded to provide a path for the zero-sequence current.

All possible open-circuit fault (OCF) scenarios and the corresponding fault-tolerant operating modes in symmetrical dual three-phase machine are shown in Table II. As shown in Table II, Scenario No. 0, 1, 2b, 2c, 3a and 4a are the normal (for No. 0) and fault-tolerant operating modes (for the others) in

TABLE II
PHASE OPEN-CIRCUIT FAULT SCENARIOS FOR SYMMETRICAL DUAL THREE-PHASE PMSM

No. OCF	No. Scenario	Open-Circuit Phases	Remaining Phase Connections	Operating Mode
Normal	0	-	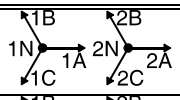	1T2T-2N
1 OCF	1	A2	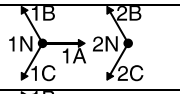	1T2D-2N
	2a	A2-B2	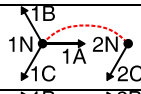	1T-1N
2 OCFs	2b	A1-A2	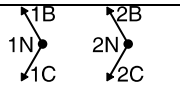	1D2D-2N
	2c	A1-B2	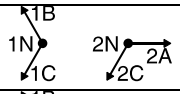	1D2D-2N
	3a	A2-B2-C2	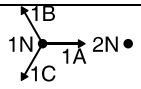	1T-2N
3 OCFs	3b	A1-B2-C2	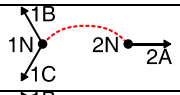	1T-1N
	3c	A1-A2-B2	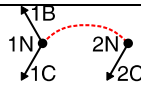	1D-1N
	4a	A1-A2-B2-C2	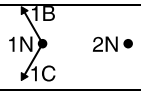	1D-2N
4 OCFs	4b	A1-B1-B2-C2	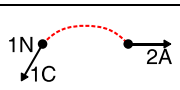	1D-1N
	4c	A1-B1-A2-B2	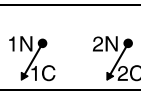	-
5 OCFs	5	A1-B1-A2-B2-C2	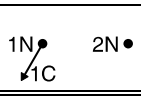	-

Note: Red dotted line indicates the connection of two neutral points. Operating mode '1T2D' means that the first three-phase winding is operated in T mode and the second one is operated in D mode; '2N' means that the neutral points of two three-phase windings are isolated, '1N' means that the neutral points of two three-phase windings are connected. Others have the similar meanings.

which two three-phase windings have the isolated neutrals. The field distribution and electromagnetic performance of these scenarios are investigated in this paper.

Scenario No. 2a, 3b, 3c and 4b are the fault-tolerant operating modes in which two three-phase windings have the connected neutrals. Therefore, an additional conductive wire is required to connect the neutral points. Among these scenarios, No. 3b and 4b are so similar to the scenarios No. 3a and No. 4a that they are not need to discussed. In No. 2a and 3c, the determination of the postfault phase currents is multiple-solution problem due to the existence of the same redundant phases. The complicated multiple-solution problem is out of scope of this paper. In No. 4c and 5, the machine cannot work since the rotating MMF cannot be maintained anymore.

So far, the general field solutions in all subdomains and the current density distribution under open-phase faulty conditions has been given. According to them, the magnetic field distribution can be completely determined under different fault-tolerant operating modes. Then, the electromagnetic performance expression will be derived in next section.

V. Electromagnetic Performance Prediction

A. Back EMF

The flux linkage of each coil can be derived from the vector potential at the center of the upper or lower layer. With the assumption that the current density is constant over the upper or lower layer of slot, the flux linkage of each coil can be represented with magnetic potential vector as

$$\lambda_{iU} = \frac{LN_t}{A_U}\int_{\theta_i-\frac{\gamma}{2}}^{\theta_i+\frac{\gamma}{2}}\int_{R_4}^{R_5} A_{IVi}(r,\theta)r\,\mathrm{d}r\,\mathrm{d}\theta \simeq LN_t A_{IVi}\left(\tfrac{R_4+R_5}{2},\theta_i\right) \quad (42)$$

$$\lambda_{iL} = \frac{LN_t}{A_L}\int_{\theta_i-\frac{\gamma}{2}}^{\theta_i+\frac{\gamma}{2}}\int_{R_5}^{R_6} A_{Vi}(r,\theta)r\,\mathrm{d}r\,\mathrm{d}\theta \simeq LN_t A_{Vi}\left(\tfrac{R_5+R_6}{2},\theta_i\right) \quad (43)$$

where L is the machine axial active length, N_t is the number of turns per coil.

Then, the back EMF vector is given by

$$\mathrm{col}(E_j)_j = \omega\frac{d}{d\theta_0}\mathrm{col}(\lambda_j)_j \quad (44)$$

$$\mathrm{col}(\lambda_j)_j = \mathbf{C}_U\cdot\mathrm{col}(\lambda_{Ui})_i + \mathbf{C}_L\cdot\mathrm{col}(\lambda_{Li})_i \quad (45)$$

where ω is the mechanical speed of the rotor, θ_0 is the rotor position mechanical angle, $\mathbf{C}_U$ and $\mathbf{C}_L$ are the connecting matrix defined in Section II.

B. Electromagnetic Torque

The electromagnetic torque can be calculated by applying the Maxwell stress tensor on the surface as

$$T_e = \frac{LR_m^2}{\mu_0}\int_0^{2\pi} B_{IIr}\big|_{r=R_m}\cdot B_{II\theta}\big|_{r=R_m}\,\mathrm{d}\theta \quad (46)$$

Substituting the air gap field solution (18) and (22) into (46), the electromagnetic torque can be simplified as

$$T_e = \frac{2\pi L}{\mu_0}\sum_{k=1}^{\infty}k^2\left(\frac{R_3}{R_2}\right)^k\left(B_{IIk}C_{IIk} - A_{IIk}D_{IIk}\right) \quad (47)$$

where $R_m = \frac{1}{2}(R_2+R_3)$ representing the radius of the mid air gap.

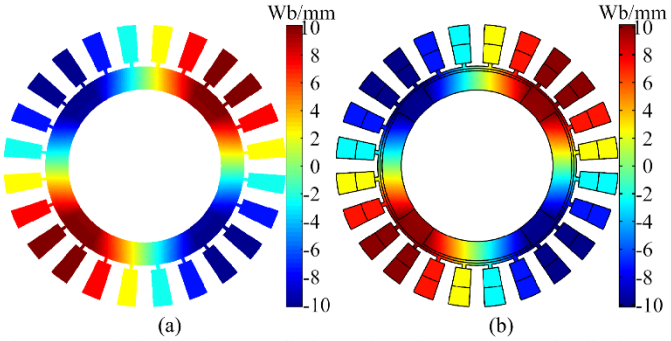

Fig. 4. Analytical and FE predictions of z-axis component distribution of magnetic potential vector. (a) Analytical result. (b) FE result.

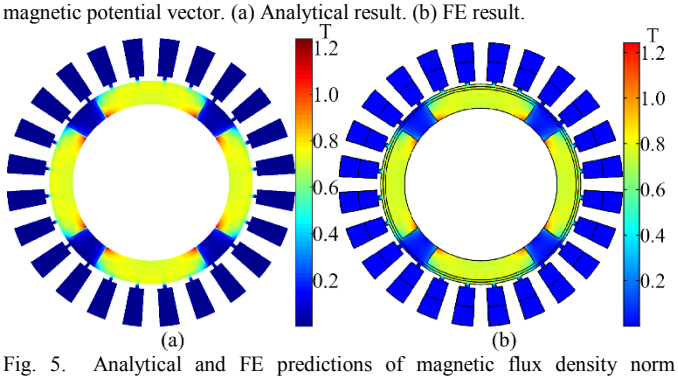

Fig. 5. Analytical and FE predictions of magnetic flux density norm distribution. (a) Analytical result. (b) FE result.

C. Unbalanced Magnetic Force

The unbalanced magnetic force acting on the rotor will appears due to the asymmetrical magnetic field. The asymmetrical magnetic field are caused by asymmetrical current distribution under fault-tolerant operating modes. In this paper, the unbalanced magnetic force is also calculated using Maxwell stress tensor. The x- and y-axis components of the unbalanced magnetic force can be expressed by [22],

$$F_x = \frac{LR_m}{\mu_0}\int_0^{2\pi}\left(\frac{1}{2}(B_{II\theta}^2 - B_{IIr}^2)\cos\theta + B_{IIr}B_{II\theta}\sin\theta\right)\Big|_{r=R_m}\mathrm{d}\theta \quad (48)$$

$$F_y = \frac{LR_m}{\mu_0}\int_0^{2\pi}\left(\frac{1}{2}(B_{II\theta}^2 - B_{IIr}^2)\sin\theta - B_{IIr}B_{II\theta}\cos\theta\right)\Big|_{r=R_m}\mathrm{d}\theta \quad (49)$$

where $R_m = \frac{1}{2}(R_2+R_3)$ representing the radius of the mid air gap.

VI. Analytical Results and Comparison with FEA

The symmetrical dual three-phase 24-slot/4-pole prototype PMSM studied in this paper is shown in Fig. 1(a) and the major parameters are listed in Table I. In order to validate the proposed model, the analytical results have been compared with 2-D finite-element results obtained using COMSOL Multiphysics™ software. The analytical and simulation results have been extensively compared under different conditions including open-circuit, armature reaction field and on-load conditions. Furthermore, armature reaction field and electromagnetic performance under different fault-tolerant operation modes have been investigated. The analytical field solutions of five subdomains are computed using Matlab™ software with finite harmonic orders K, M and N for Region

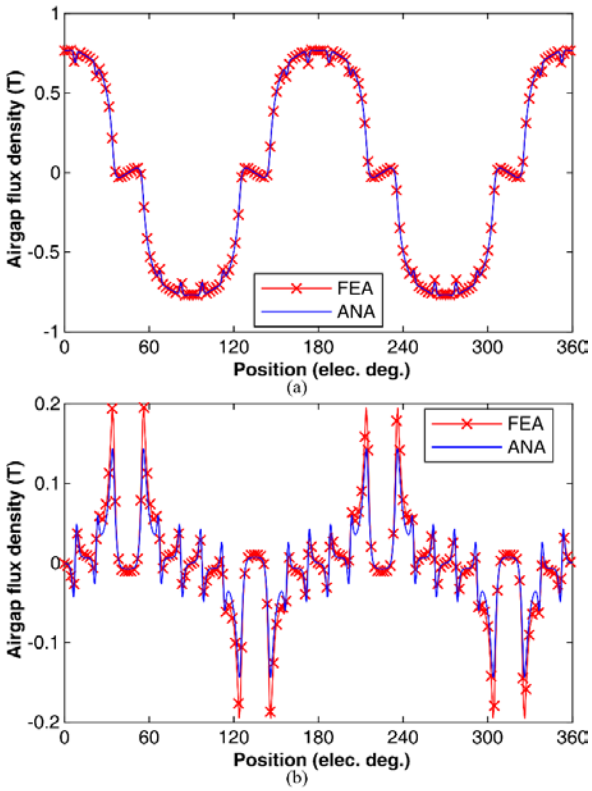

Fig. 6. Analytical and FE predicted air-gap flux density waveforms in the middle of the air-gap. (a) Radial component. (b) Tangential component.

I/*II*, Region *IIIi* and Region *IVi*/*Vi*, respectively. The maximum harmonic orders K, M and N are shown in Table I.

A. Open-circuit Condition

Fig. 4 shows the z-axis component distribution of the magnetic potential vector in all five subdomains. Fig. 5 shows the magnetic flux density norm distribution in those subdomains. It is apparent from these results that good agreement is achieved between the analytical and the FE results.

The radial and tangential component of the flux density distribution in the middle of the air-gap are shown in Fig. 6. The effect of slots on the flux density distributions can be observed clearly, for both the radial and tangential components of air-gap flux density. As seen in Fig. 4, 5 and 6, a good agreement is achieved between the analytical and FE results. However, the tangential component of flux density obtained by FEA is slightly higher than that obtained by analytical model.

Fig. 7 shows the comparison between the analytical predicted and FE-simulated phase back-EMFs for the 4-pole/24-slot symmetrical dual three-phase PMSM. The computation is done at the rated mechanical speed 3 000 rpm. The analytical results provide a good agreement with those of the FE method. As also seen from Fig. 7, The magnitude and phase of the corresponding phase back-EMFs of the symmetrical dual three-phase machine are the same. Fig. 8 shows the analytical predicted and FE-simulated cogging torques for this machine. The cogging torque is repeated every 30 elec. degree because the largest common multiple of pole number $2p$, and slot number N_s, is 24, which yields the period of the cogging torque $p \times 360°/24 = 30°$. The cogging torque waveforms obtained by analytical model and FEA are almost the same. However, it

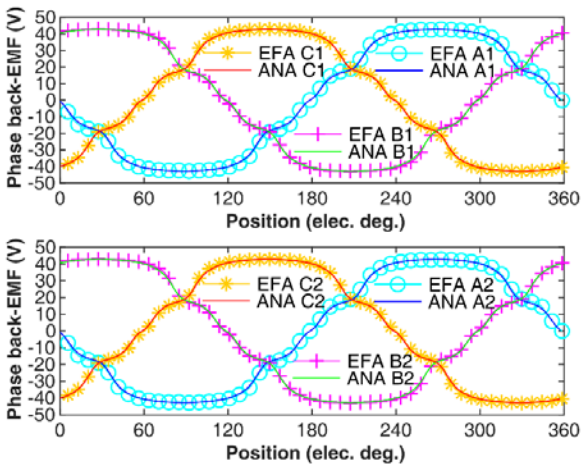

Fig. 7. Analytical and FE predictions of phase back-EMF in the 4-pole/24-slot symmetrical dual three-phase PMSM.

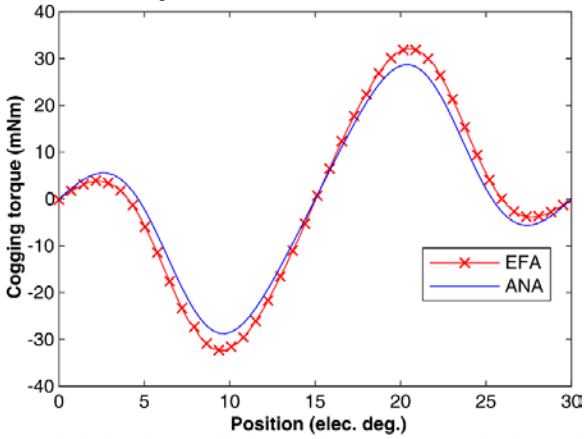

Fig. 8. Analytical and FE predictions of the cogging torque in the 4-pole/24-slot symmetrical dual three-phase PMSM.

should be noted that the magnitude of the analytical predicted cogging torque is about 10% lower than the FE-simulated one.

B. Armature Reaction Field

Fig. 9 shows the flux distribution under different operation modes listed in Table II. Each subfigure depicts the situation that rotor mechanical angle is 0 and $\pi/2$, from left to right respectively. Fig. 9(a) shows the flux distribution under no-load condition, under which the magnetic field only caused by the PMs. Fig. 9(b)–(g) show the flux distribution caused by the armature reaction acting alone under the scenario 0, 1, 2b, 2c, 3a and 4a listed in Table II, respectively. In Fig. 9(b)–(g), the magnets are considered to be completely unmagnetized and have no effect on the field distribution. Among these scenarios, scenario 0 is the normal operation mode whereas other scenarios are the fault-tolerant operation modes withstanding one and up to four phases open-circuit faults. The phase currents are winding current density distribution for different operation modes have been discussed in Section IV.

Fig. 10 depicts the radial and tangential components of the armature reaction flux density distribution in the middle of the air-gap under different operation modes. Fig. 10(a)–(f) show the air-gap flux distribution caused by the armature reaction acting alone under the scenario No. 0, 1, 2b, 2c, 3a and 4a listed in Table II, respectively. It is clearly observable that the analytical results show a good agreement with those obtained

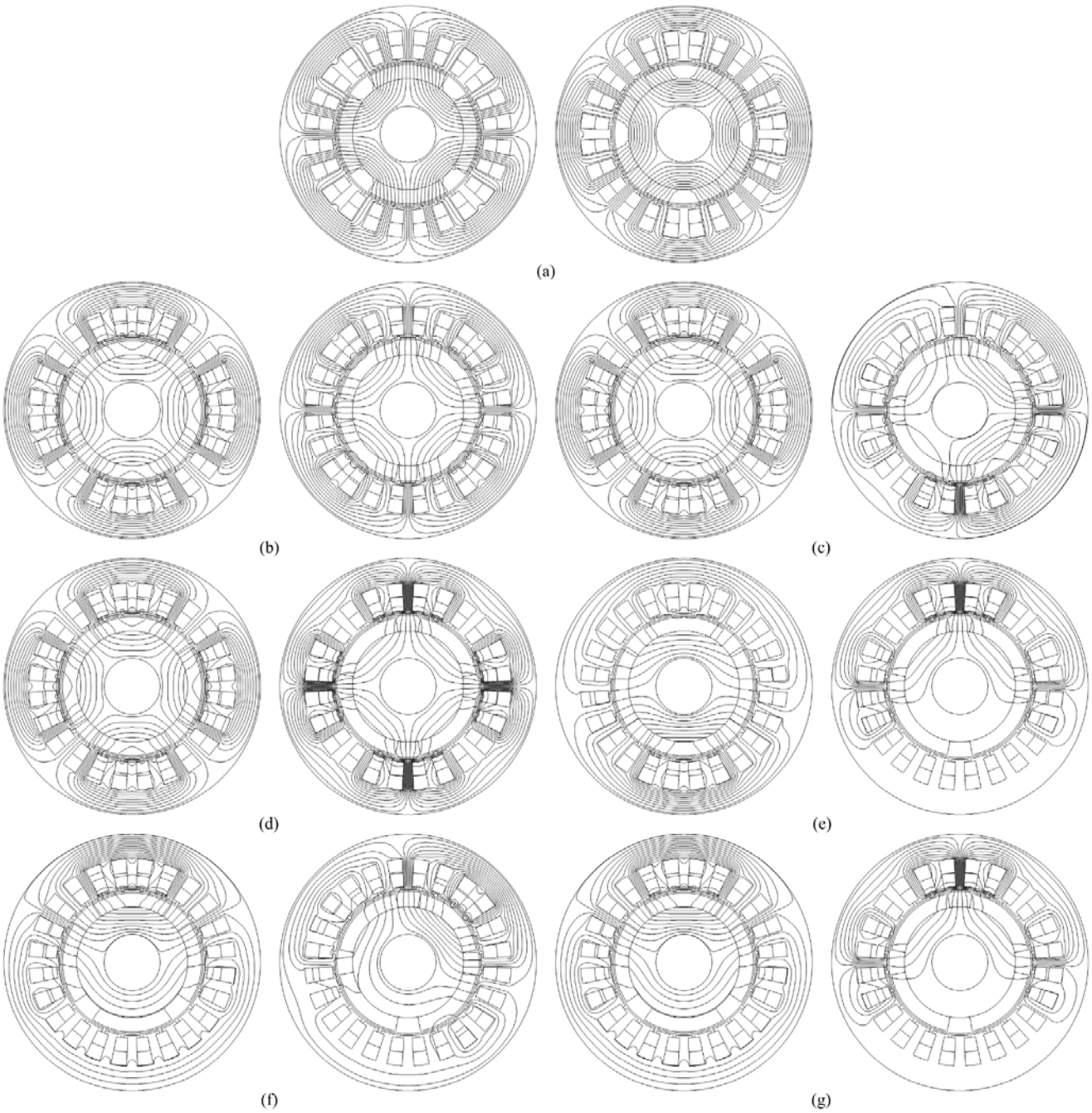

Fig. 9. No-load and armature reaction magnetic flux distribution for normal and open-circuit fault operation modes. (a) Flux distribution caused by PMs alone. (b)–(g) Armature reaction flux distribution under different operations: (b) Normal operation (Scenarios 0); (c) Phase-$a2$ is open-circuit (Scenarios 1); (d) Phase-$a1$ and -$a2$ are open-circuit (Scenarios 2b); (e) Phase-$a1$ and -$b2$ are open-circuit (Scenarios 2c); (f) Phase-$a2$, -$b2$ and -$c2$ are open-circuit (Scenarios 3a); (g) Phase-$a1$, -$a2$, -$b2$ and -$c2$ are open-circuit (Scenarios 4a). Each of subfigures depicts the flux distribution when the rotor angle is 0 and $\pi/2$, from left to right respectively

by FEA under all fault-tolerant operation modes.

Moreover, the effect of slots on the armature reaction flux density can be seen in Fig. 10.

As seen in Fig. 9 and Fig. 10, only scenario 0 (Fig. 9(b) and Fig. 10(a)) and scenario 2b (Fig. 9(d) and Fig. 10(c)) have the symmetrical armature reaction flux distribution. It means that unbalanced magnetic force will appears in other asymmetrical fault-tolerant operating modes. The unbalanced magnetic force under different operation modes will be investigated in next subsection.

C. Torque and Unbalanced Magnetic Force

Fig. 11 gives the comparisons between the analytical predicted and FE-simulated torque under different operation modes. All analytical results provide a good agreement with those of the FE method. As seen in Fig. 11, all fault-tolerant operation modes can provide average torque. However, the average torque under scenarios 3a and 4a is only the half of that under normal operation because only one three-phase winding works under these conditions. Therefore, in order to provide the rated torque as the normal condition, the remaining healthy phase currents under scenarios 3a and 4a must be doubled, which inevitably increases the machine heat loading.

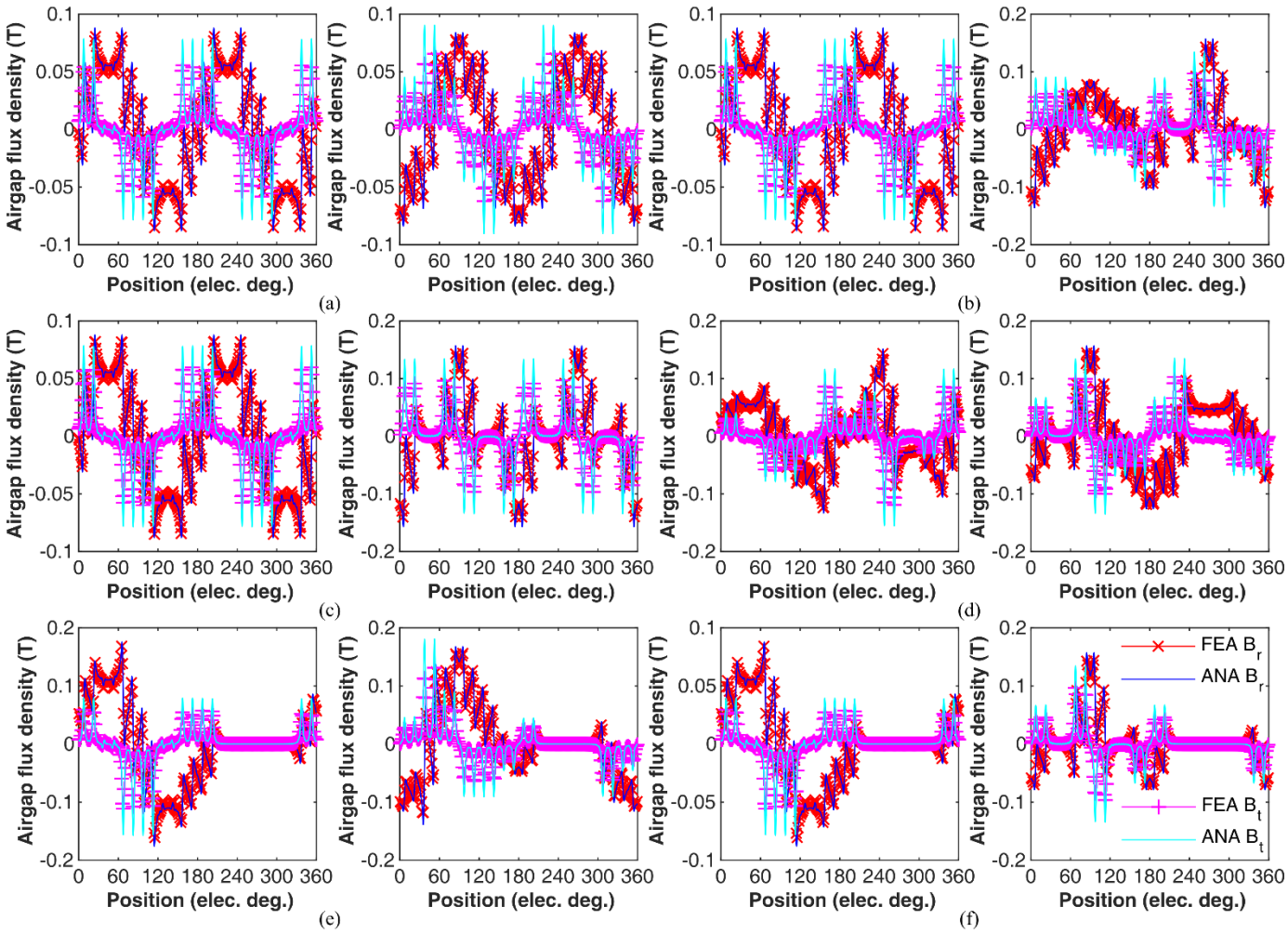

Fig. 10. Radial and tangential components of the armature reaction flux density in the middle of the air-gap under normal and open-circuit fault operation modes. (a) Normal operation (Scenarios 0); (b) Phase-$a2$ is open-circuit (Scenarios 1); (c) Phase-$a1$ and -$a2$ are open-circuit (Scenarios 2b); (d) Phase-$a1$ and -$b2$ are open-circuit (Scenarios 2c); (e) Phase-$a2$, -$b2$ and -$c2$ are open-circuit (Scenarios 3a); (f) Phase-$a1$, -$a2$, -$b2$ and -$c2$ are open-circuit (Scenarios 4a). Each of subfigures depicts the flux distribution when the rotor angle is 0 and $\pi/2$, from left to right respectively.

TABLE III
TORQUE AND UMF PREDICTIONS UNDER DIFFERENT PHASE OPEN-CIRCUIT FAULT SCENARIOS

No. Scenario	Phase Current of Winding #1	Phase Current of Winding #2	Average Torque	Torque Ripples	Average x-axis UMF	x-axis UMF Ripples	Average y-axis UMF	y-axis UMF Ripples
0	5.3 A (1 p.u.)	5.3 A (1 p.u.)	3.2 Nm (1 p.u.)	0.42 Nm (13.1%)	0	0	0	0
1	5.3 A (1 p.u.)	9.15 A (1.732 p.u.)	3.2 Nm (1 p.u.)	0.65 Nm (20.0%)	-13.44 N	47.87 N	2.32 N	13.84 N
2b	9.15 A (1.732 p.u.)	9.15 A (1.732 p.u.)	3.2 Nm (1 p.u.)	0.90 Nm (28.1%)	0	0	0	0
2c	9.15 A (1.732 p.u.)	9.15 A (1.732 p.u.)	3.2 Nm (1 p.u.)	0.57 Nm (17.8%)	3.56 N	86.18 N	3.08 N	25.34 N
3a	5.3 A (1 p.u.)	0	1.6 Nm (0.5 p.u.)	0.23 Nm (14.4%)	-19.02 N	102 N	-7.97 N	36.28 N
4a	9.15 A (1.732 p.u.)	0	1.6 Nm (0.5 p.u.)	0.46 Nm (28.9%)	3.98 N	49.88 N	-3.27 N	12.32 N

As seen in Fig. 11, torque ripples when the machine operated in two-phase mode (shown in Fig. 11(b), (c), (d) and (f)) are higher than that in three-phase mode (shown in Fig. 11(a) and (e)). The period of the torque fluctuation under T mode is $1/6$ of the electrical period of machine whereas the period of the torque ripples under D mode is $1/2$ of the electrical period. The torque ripples are mainly caused by the effect of slots and third harmonic air-gap flux under three-phase mode and those under two-phase mode are caused by not only the effect of slots but also the interaction between asymmetrical phase currents and the third harmonic air-gap flux.

Fig. 12 shows the unbalanced magnetic force under different operation modes. The results demonstrate that all subdomain models achieve similar waveforms as FEA.

Finally, comprehensive results about electromagnetic torque and unbalanced magnetic force under different open-circuit scenarios are given in Table III.

VII. CONCLUSION

An analytical subdomain model for the dual three-phase surface-mounted PM machines with symmetrical overlapping winding configuration has been presented in the paper for predicting the electromagnetic performance under open-phase faulty conditions. The whole domain is divided into five regions,

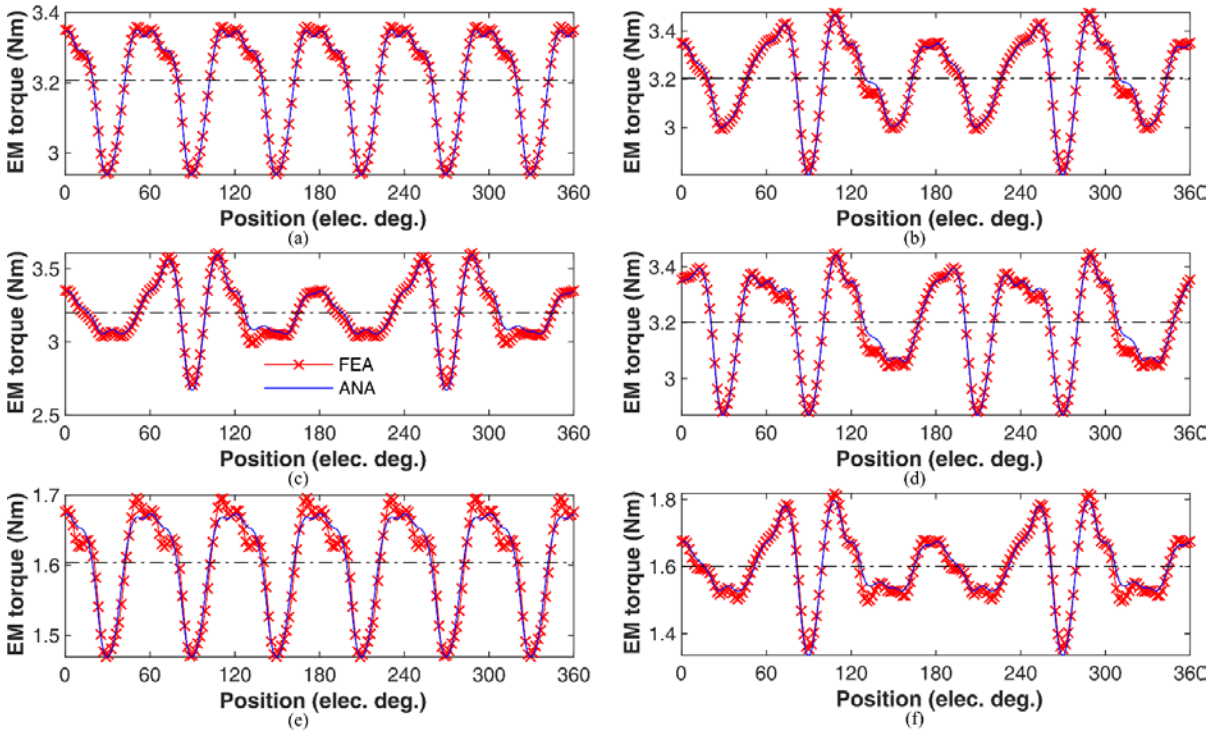

Fig. 11. Analytical and FE predictions of electromagnetic torque under normal and open-circuit fault operation modes. (a) Normal operation (Scenarios 0); (b) Phase-$a2$ is open-circuit (Scenarios 1); (c) Phase-$a1$ and -$a2$ are open-circuit (Scenarios 2b); (d) Phase-$a1$ and -$b2$ are open-circuit (Scenarios 2c); (e) Phase-$a2$, -$b2$ and -$c2$ are open-circuit (Scenarios 3a); (f) Phase-$a1$, -$a2$, -$b2$ and -$c2$ are open-circuit (Scenarios 4a).

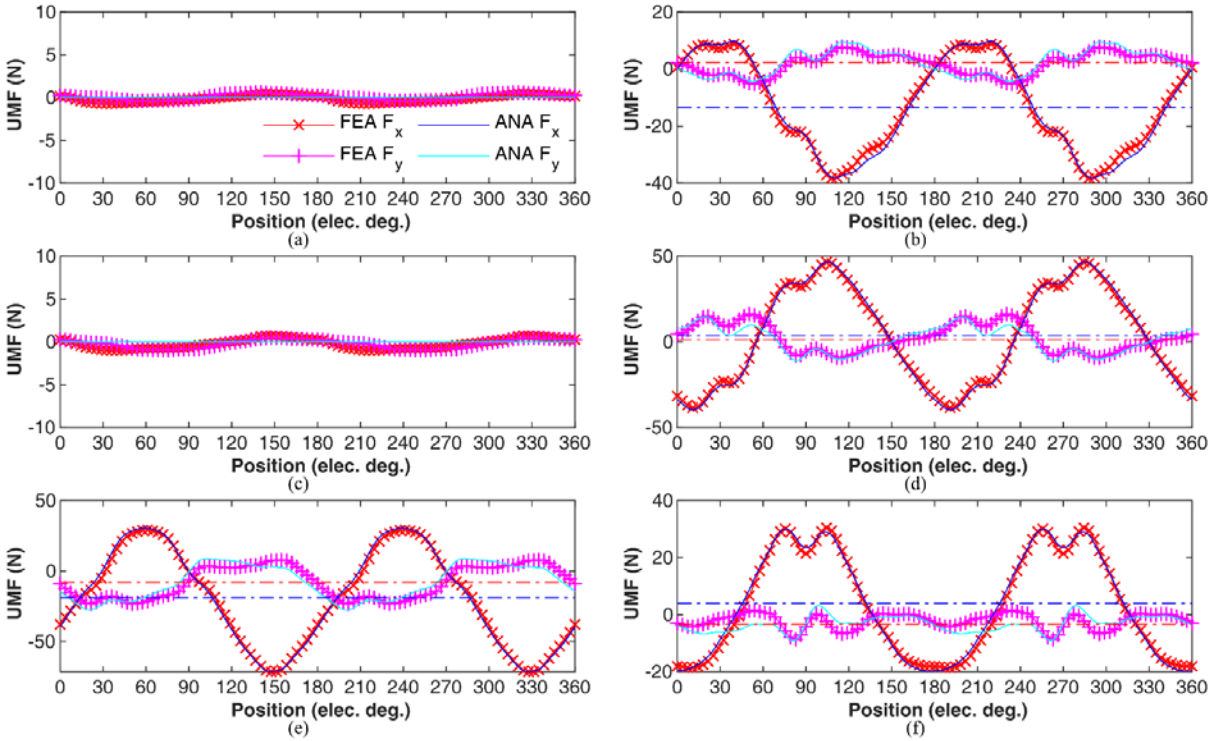

Fig. 12. Analytical and FE predictions of unbalanced magnetic force under normal and open-circuit fault operation modes. (a) Normal operation (Scenarios 0); (b) Phase-$a2$ is open-circuit (Scenarios 1); (c) Phase-$a1$ and -$a2$ are open-circuit (Scenarios 2b); (d) Phase-$a1$ and -$b2$ are open-circuit (Scenarios 2c); (e) Phase-$a2$, -$b2$ and -$c2$ are open-circuit (Scenarios 3a); (f) Phase-$a1$, -$a2$, -$b2$ and -$c2$ are open-circuit (Scenarios 4a).

viz. PMs, air-gap, slot-openings, upper- and lower-layer slots. Based on the established analytical model with sufficient derivations, the electromagnetic performance, such as the electromagnetic torque and the unbalanced magnetic force, under different open-phase fault-tolerant operating modes have been predicted. The analytically predicted results have been compared with those from FEA. Good agreements have been achieved between analytical and FEA results. Furthermore, a comprehensive investigation result about electromagnetic torque and unbalanced magnetic force under different open-phase situations has been provided in Table III. It worth noting that the proposed analytical model can be easily extended to

the symmetrical dual three-phase PM machines with any slot and pole combination though 24-slot/4-pole model used in this paper. Therefore, the analytical model can be used to accurately predict the postfault electromagnetic performance under open-phase conditions.

APPENDIX

We define the following inner products $(\cdot,\cdot)_{[\theta_i-\beta/2,\theta_i+\beta/2]}$ on the Hilbert space $\mathcal{L}^2[\theta_i-\beta/2,\theta_i+\beta/2]$ as

$$c_0(i,k)=\left(\cos_k,1\right)_{[\theta_i-\beta/2,\theta_i-\beta/2]}=\int_{\theta_i-\beta/2}^{\theta_i-\beta/2}\cos k\theta\,\mathrm{d}\theta \tag{50}$$

$$s_0(i,k)=\left(\sin_k,1\right)_{[\theta_i-\beta/2,\theta_i-\beta/2]}=\int_{\theta_i-\beta/2}^{\theta_i-\beta/2}\sin k\theta\,\mathrm{d}\theta \tag{51}$$

$$\begin{aligned}c(i,k,m)&=\left(\cos_k,\cos_{\nu_m}\right)_{[\theta_i-\beta/2,\theta_i-\beta/2]}\\&=\int_{\theta_i-\beta/2}^{\theta_i-\beta/2}\cos k\theta\cos\nu_m\left(\theta-\theta_i+\frac{\beta}{2}\right)\mathrm{d}\theta\end{aligned} \tag{52}$$

$$\begin{aligned}s(i,k,m)&=\left(\sin_k,\cos_{\nu_m}\right)_{[\theta_i-\beta/2,\theta_i-\beta/2]}\\&=\int_{\theta_i-\beta/2}^{\theta_i-\beta/2}\sin k\theta\cos\nu_m\left(\theta-\theta_i+\frac{\beta}{2}\right)\mathrm{d}\theta\end{aligned} \tag{53}$$

$$g(i,n)=\left(\cos_{\omega_n},1\right)_{[\theta_i-\beta/2,\theta_i-\beta/2]}=\int_{\theta_i-\beta/2}^{\theta_i-\beta/2}\cos\omega_n\left(\theta-\theta_i+\frac{\gamma}{2}\right)d\theta \tag{54}$$

$$\begin{aligned}h(i,m,n)&=\left(\cos_{\omega_n},\cos_{\nu_m}\right)_{[\theta_i-\beta/2,\theta_i-\beta/2]}\\&=\int_{\theta_i-\beta/2}^{\theta_i-\beta/2}\cos\omega_n\left(\theta-\theta_i+\frac{\gamma}{2}\right)\cos\nu_m\left(\theta-\theta_i+\frac{\beta}{2}\right)d\theta\end{aligned} \tag{55}$$

A. Interface between the PM Region and the Air-Gap Region

$$\begin{aligned}&A_{Ik}G_{1k}(R_2)+\frac{\mu_0}{k^2-1}\left(G_{2k}(R_2)M_{\theta ck}-G_{3k}(R_2)M_{rsk}\right)\\&=A_{IIk}+B_{IIk}\left(\frac{R_3}{R_2}\right)^k\end{aligned} \tag{56}$$

$$\begin{aligned}&C_{Ik}G_{1k}(R_2)+\frac{\mu_0}{k^2-1}\left(G_{2k}(R_2)M_{\theta sk}+G_{3k}(R_2)M_{rck}\right)\\&=C_{IIk}+D_{IIk}\left(\frac{R_3}{R_2}\right)^k\end{aligned} \tag{57}$$

$$\begin{aligned}&A_{Ik}\left(\left(\frac{R_2}{R_1}\right)^k-\left(\frac{R_1}{R_2}\right)^k\right)+\frac{\mu_0R_2}{k^2-1}\left(1-\left(\frac{R_1}{R_2}\right)^{k+1}\right)\left(kM_{\theta ck}-M_{rsk}\right)\\&=\mu_r\left(A_{IIk}-B_{IIk}\left(\frac{R_3}{R_2}\right)^k\right)\end{aligned} \tag{58}$$

$$\begin{aligned}&C_{Ik}\left(\left(\frac{R_2}{R_1}\right)^k-\left(\frac{R_1}{R_2}\right)^k\right)+\frac{\mu_0R_2}{k^2-1}\left(1-\left(\frac{R_1}{R_2}\right)^{k+1}\right)\left(kM_{\theta sk}+M_{rck}\right)\\&=\mu_r\left(C_{IIk}-D_{IIk}\left(\frac{R_3}{R_2}\right)^k\right)\end{aligned} \tag{59}$$

(56)–(59) can be rewritten into matrix format as

$$\mathbf{T_{11}A_I}+\mathbf{T_{13}A_{II}}+\mathbf{T_{14}B_{II}}=\mathbf{Y_1} \tag{60}$$

$$\mathbf{T_{22}C_I}+\mathbf{T_{25}C_{II}}+\mathbf{T_{26}D_{II}}=\mathbf{Y_2} \tag{61}$$

$$\mathbf{T_{31}A_I}+\mathbf{T_{33}A_{II}}+\mathbf{T_{34}B_{II}}=\mathbf{Y_3} \tag{62}$$

$$\mathbf{T_{42}C_I}+\mathbf{T_{45}C_{II}}+\mathbf{T_{46}D_{II}}=\mathbf{Y_4} \tag{63}$$

where

$$\mathbf{T_{11}}=\mathbf{T_{22}}=\mathrm{diag}\left(\left(\frac{R_2}{R_1}\right)^k+\left(\frac{R_1}{R_2}\right)^k\right)_k$$

$$\mathbf{T_{13}}=\mathbf{T_{25}}=\mathrm{diag}(-1)_K$$

$$\mathbf{T_{14}}=\mathbf{T_{26}}=\mathrm{diag}\left(-\left(\frac{R_3}{R_2}\right)^k\right)_k$$

$$\mathbf{T_{31}}=\mathbf{T_{42}}=\mathrm{diag}\left(\frac{1}{\mu_r}\frac{k}{R_2}\left(\left(\frac{R_2}{R_1}\right)^k-\left(\frac{R_1}{R_2}\right)^k\right)\right)_k$$

$$\mathbf{T_{33}}=\mathbf{T_{45}}=\mathrm{diag}\left(-\frac{k}{R_2}\right)_k$$

$$\mathbf{T_{34}}=\mathbf{T_{46}}=\mathrm{diag}\left(\frac{k}{R_2}\left(\frac{R_3}{R_2}\right)^k\right)_k$$

$$\mathbf{Y_1}=\mathrm{diag}\left(-\frac{\mu_0}{k^2-1}\begin{pmatrix}\left(R_2+kR_1\left(\frac{R_1}{R_2}\right)^k\right)M_{\theta ck}\\-\left(kR_2+R_1\left(\frac{R_1}{R_2}\right)^k\right)M_{rsk}\end{pmatrix}\right)_k$$

$$\mathbf{Y_2}=\mathrm{diag}\left(-\frac{\mu_0}{k^2-1}\begin{pmatrix}\left(R_2+kR_1\left(\frac{R_1}{R_2}\right)^k\right)M_{\theta sk}\\+\left(kR_2+R_1\left(\frac{R_1}{R_2}\right)^k\right)M_{rck}\end{pmatrix}\right)_k$$

$$\mathbf{Y_3}=\mathrm{diag}\left(-\frac{\mu_0k}{\mu_r\left(k^2-1\right)}\left(\left(1-\left(\frac{R_1}{R_2}\right)^{k+1}\right)\left(kM_{\theta ck}-M_{rsk}\right)\right)\right)_k$$

$$\mathbf{Y_4}=\mathrm{diag}\left(-\frac{\mu_0k}{\mu_r\left(k^2-1\right)}\left(\left(1-\left(\frac{R_1}{R_2}\right)^{k+1}\right)\left(kM_{\theta sk}+M_{rck}\right)\right)\right)_k$$

B. Interface between the Air-Gap Region and Slot-Openning Region

$$\sum_{k=1}^{K}\left(\left(A_{IIk}\left(\frac{R_3}{R_2}\right)^k+B_{IIk}\right)\frac{c_0(i,k)}{\beta}+\left(C_{IIk}\left(\frac{R_3}{R_2}\right)^k+D_{IIk}\right)\frac{s_0(i,k)}{\beta}\right) \quad (64)$$
$$=A_{IIIi,0}+B_{IIIi,0}\ln R_3$$

$$\sum_{k=1}^{K}\left(\left(A_{IIk}\left(\frac{R_3}{R_2}\right)^k+B_{IIk}\right)\frac{c(i,k,m)}{\beta/2}+\left(C_{IIk}\left(\frac{R_3}{R_2}\right)^k+D_{IIk}\right)\frac{s(i,k,m)}{\beta/2}\right) \quad (65)$$
$$=A_{IIIi,m}+B_{IIIi,m}\left(\frac{R_4}{R_3}\right)^{\nu_m}$$

$$\frac{k}{R_3}\left(A_{IIk}\left(\frac{R_3}{R_2}\right)^k-B_{IIk}\right)=\sum_{i=1}^{N_s}\frac{B_{IIIi,0}}{R_3}\frac{c_0(i,k)}{\pi} +\sum_{i=1}^{N_s}\sum_{m=1}^{M}\frac{\nu_m}{R_3}\left(A_{IIIi,m}-B_{IIIi,m}\left(\frac{R_4}{R_3}\right)^{\nu_m}\right)\frac{c(i,k,m)}{\pi} \quad (66)$$

$$\frac{k}{R_3}\left(C_{IIk}\left(\frac{R_3}{R_2}\right)^k-D_{IIk}\right)=\sum_{i=1}^{N_s}\frac{B_{IIIi,0}}{R_3}\frac{s_0(i,k)}{\pi} +\sum_{i=1}^{N_s}\sum_{m=1}^{M}\frac{\nu_m}{R_3}\left(A_{IIIi,m}-B_{IIIi,m}\left(\frac{R_4}{R_3}\right)^{\nu_m}\right)\frac{s(i,k,m)}{\pi} \quad (67)$$

(64)–(67) can be rewritten into matrix format as

$$\mathbf{T_{53}A_{II}}+\mathbf{T_{54}B_{II}}+\mathbf{T_{55}C_{II}}+\mathbf{T_{56}D_{II}}+\mathbf{T_{57}A_{III}}+\mathbf{T_{58}B_{III}}=\mathbf{0} \quad (68)$$

$$\mathbf{T_{63}A_{II}}+\mathbf{T_{64}B_{II}}+\mathbf{T_{67}A_{III}}+\mathbf{T_{68}B_{III}}=\mathbf{0} \quad (69)$$

$$\mathbf{T_{75}C_{II}}+\mathbf{T_{76}D_{II}}+\mathbf{T_{77}A_{III}}+\mathbf{T_{78}B_{III}}=\mathbf{0} \quad (70)$$

where

$$\mathbf{T_{53}}=\mathrm{col}\left(\frac{\mathrm{row}\left(\left(\frac{R_3}{R_2}\right)^k\frac{c_0(i,k)}{\beta}\right)_k}{\left[\left(\frac{R_3}{R_2}\right)^k\frac{c(i,k,m)}{\beta/2}\right]_{m,k}}\right)_i$$

$$\mathbf{T_{54}}=\mathrm{col}\left(\frac{\mathrm{row}\left(\frac{c_0(i,k)}{\beta}\right)_k}{\left[\frac{c(i,k,m)}{\beta/2}\right]_{m,k}}\right)_i$$

$$\mathbf{T_{55}}=\mathrm{col}\left(\frac{\mathrm{row}\left(\left(\frac{R_3}{R_2}\right)^k\frac{s_0(i,k)}{\beta}\right)_k}{\left[\left(\frac{R_3}{R_2}\right)^k\frac{s(i,k,m)}{\beta/2}\right]_{m,k}}\right)_i$$

$$\mathbf{T_{56}}=\mathrm{col}\left(\frac{\mathrm{row}\left(\frac{s_0(i,k)}{\beta}\right)_k}{\left[\frac{s(i,k,m)}{\beta/2}\right]_{m,k}}\right)_i$$

$$\mathbf{T_{57}}=\mathrm{diag}(-1)_{(M+1)N_s\times(M+1)}$$

$$\mathbf{T_{58}}=\mathrm{diag}\left(\left.\begin{array}{c|c}-\ln R_3 & \mathbf{0}\\ \hline \mathbf{0} & \mathrm{diag}\left(-\left(\frac{R_4}{R_3}\right)^{\nu_m}\right)_m\end{array}\right)_i$$

$$\mathbf{T_{63}}=\mathbf{T_{75}}=\mathrm{diag}\left(\frac{k}{R_3}\left(\frac{R_3}{R_2}\right)^k\right)_k$$

$$\mathbf{T_{64}}=\mathbf{T_{76}}=\mathrm{diag}\left(-\frac{k}{R_3}\right)_k$$

$$\mathbf{T_{67}}=\mathrm{row}\left(\mathbf{0}\ \middle|\ \left[-\frac{\nu_m}{R_3}\frac{c(i,k,m)}{\pi}\right]_{k,m}\right)_i$$

$$\mathbf{T_{68}}=\mathrm{row}\left(\mathrm{col}\left(-\frac{1}{R_3}\frac{c_0(i,k)}{\pi}\right)_k\ \middle|\ \left[\frac{\nu_m}{R_3}\left(\frac{R_4}{R_3}\right)^{\nu_m}\frac{c(i,k,m)}{\pi}\right]_{k,m}\right)_i$$

$$\mathbf{T_{77}}=\mathrm{row}\left(\mathbf{0}\ \middle|\ \left[-\frac{\nu_m}{R_3}\frac{s(i,k,m)}{\pi}\right]_{k,m}\right)_i$$

$$\mathbf{T_{78}}=\mathrm{row}\left(\mathrm{col}\left(-\frac{1}{R_3}\frac{s_0(i,k)}{\pi}\right)_k\ \middle|\ \left[\frac{\nu_m}{R_3}\left(\frac{R_4}{R_3}\right)^{\nu_m}\frac{s(i,k,m)}{\pi}\right]_{k,m}\right)_i$$

C. Interface between the Slot-Opening Region and Slot Upper-Layer Region

$$A_{IVi,0}+B_{IVi,0}\ln R_4-\frac{1}{4}\mu_0J_{Ui}R_4^2 +\sum_{n=1}^{N}\left(A_{IVi,n}+B_{IVi,n}\left(\frac{R_5}{R_4}\right)^{\omega_n}\right)\frac{g(i,n)}{\beta}=A_{IIIi,0}+B_{IIIi,0}\ln R_4 \quad (71)$$

$$\sum_{n=1}^{N}\left(A_{IVi,n}+B_{IVi,n}\left(\frac{R_5}{R_4}\right)^{\omega_n}\right)\frac{h(i,m,n)}{\beta/2} =A_{IIIi,m}\left(\frac{R_4}{R_3}\right)^{\nu_m}+B_{IIIi,m} \quad (72)$$

$$\frac{B_{IVi,0}}{R_4}-\frac{1}{2}\mu_0J_{Ui}R_4 =\frac{B_{IIIi,0}}{R_4}\frac{\beta}{\gamma}+\sum_{m=1}^{M}\left(A_{IIIi,m}\frac{\nu_m}{R_4}\left(\frac{R_4}{R_3}\right)^{\nu_m}-B_{IIIi,m}\frac{\nu_m}{R_4}\right) \quad (73)$$

$$\frac{\omega_n}{R_4}\left(A_{IVi,n}-B_{IVi,n}\left(\frac{R_5}{R_4}\right)^{\omega_n}\right)=\frac{B_{IIIi,0}}{R_4}\frac{g(i,n)}{\gamma/2} +\sum_{m=1}^{M}\frac{\gamma_m}{R_4}\left(A_{IIIi,m}\left(\frac{R_4}{R_3}\right)^{\gamma_m}-B_{IIIi,m}\right)\frac{h(i,m,n)}{\gamma/2} \quad (74)$$

(71)–(74) can be rewritten into matrix format as

$$\mathbf{T_{87}A_{III}}+\mathbf{T_{88}B_{III}}+\mathbf{T_{89}A_{IV}}+\mathbf{T_{8,10}B_{IV}}=\mathbf{Y_8} \quad (75)$$

$$\mathbf{T_{97}A_{III}}+\mathbf{T_{98}B_{III}}+\mathbf{T_{99}A_{IV}}+\mathbf{T_{9,10}B_{IV}}=\mathbf{Y_9} \quad (76)$$

where

$$\mathbf{T_{87}}=\mathrm{diag}\left(\left.\begin{array}{c|c}-1 & \mathbf{0}\\ \hline \mathbf{0} & \mathrm{diag}\left(-\left(\frac{R_4}{R_3}\right)^{\nu_m}\right)_m\end{array}\right)_i$$

$$\mathbf{T_{88}}=\mathrm{diag}\left(\left.\begin{array}{c|c}-\ln R_4 & \mathbf{0}\\ \hline \mathbf{0} & \mathrm{diag}(-1)_M\end{array}\right)_i$$

$$\mathbf{T_{89}}=\mathrm{diag}\left(\left.\begin{array}{c|c}1 & \mathrm{row}\left(\frac{g(i,n)}{\beta}\right)_n\\ \hline \mathbf{0} & \left[\frac{h(i,m,n)}{\beta/2}\right]_{m,n}\end{array}\right)_i$$

$$\mathbf{T_{8,10}}=\mathrm{diag}\left(\left.\begin{array}{c|c}\ln R_4 & \mathrm{row}\left(\left(\frac{R_5}{R_4}\right)^{\omega_n}\frac{g(i,n)}{\beta}\right)_n\\ \hline \mathbf{0} & \left[\left(\frac{R_5}{R_4}\right)^{\omega_n}\frac{h(i,m,n)}{\beta/2}\right]_{m,n}\end{array}\right)_i$$

$$\mathbf{T_{97}}=\mathrm{diag}\left(\left.\begin{array}{c|c}0 & \mathbf{0}\\ \hline \mathbf{0} & \left[-\frac{\nu_m}{R_4}\left(\frac{R_4}{R_3}\right)^{\nu_m}\frac{h(i,m,n)}{\gamma/2}\right]_{n,m}\end{array}\right)_i$$

$$\mathbf{T_{98}}=\mathrm{diag}\left(\left.\begin{array}{c|c}-\frac{1}{R_4} & \mathbf{0}\\ \hline \mathbf{0} & \left[\frac{\nu_m}{R_4}\frac{h(i,m,n)}{\gamma/2}\right]_{n,m}\end{array}\right)_i$$

$$\mathbf{T_{99}}=\mathrm{diag}\left(\left.\begin{array}{c|c}0 & \mathbf{0}\\ \hline \mathbf{0} & \mathrm{diag}\left(\frac{\omega_n}{R_4}\right)_n\end{array}\right)_i$$

$$\mathbf{T_{9,10}}=\mathrm{diag}\left(\left.\begin{array}{c|c}\frac{1}{R_4} & \mathbf{0}\\ \hline \mathbf{0} & \mathrm{diag}\left(-\frac{\omega_n}{R_4}\left(\frac{R_5}{R_4}\right)^{\omega_n}\right)_n\end{array}\right)_i$$

$$\mathbf{Y_8}=\mathrm{diag}\left(\left.\begin{array}{c}\frac{1}{4}\mu_0 J_{Ui}R_4^2\\ \hline \mathbf{0}\end{array}\right)_i$$

$$\mathbf{Y_9}=\mathrm{diag}\left(\left.\begin{array}{c}\frac{1}{2}\mu_0 J_{Ui}R_4\\ \hline \mathbf{0}\end{array}\right)_i$$

D. Interface between the Slot Upper Layer Region and Lower Layer Region

$$\begin{aligned}&A_{IVi,0}+B_{IVi,0}\ln R_5-\frac{1}{4}\mu_0 J_{Ui}R_5^2\\&=A_{Vi,0}+\frac{1}{2}\mu_0 J_{Li}R_6^2\ln R_5-\frac{1}{4}\mu_0 J_{Li}R_5^2\end{aligned}\tag{77}$$

$$A_{IVi,n}\left(\frac{R_5}{R_4}\right)^{\omega_n}+B_{IVi,n}=A_{Vi,n}\left(1+\left(\frac{R_6}{R_5}\right)^{2\omega_n}\right)\tag{78}$$

$$\frac{B_{IVi,0}}{R_5}-\frac{1}{2}\mu_0 J_{Ui}R_5=\frac{1}{2}\mu_0 J_{Li}\frac{R_6^2}{R_5}-\frac{1}{2}\mu_0 J_{Li}R_5\tag{79}$$

$$\frac{\omega_n}{R_5}\left(A_{IVi,n}\left(\frac{R_5}{R_4}\right)^{\omega_n}-B_{IVi,n}\right)=A_{Vi,n}\frac{\omega_n}{R_5}\left(1-\left(\frac{R_6}{R_5}\right)^{2\omega_n}\right)\tag{80}$$

(77)–(80) can be rewritten into matrix format as

$$\mathbf{T_{10,9}A_{IV}}+\mathbf{T_{10,10}B_{IV}}+\mathbf{T_{10,11}A_V}=\mathbf{Y_{10}}\tag{81}$$

$$\mathbf{T_{11,9}A_{IV}}+\mathbf{T_{11,10}B_{IV}}+\mathbf{T_{11,11}A_V}=\mathbf{Y_{11}}\tag{82}$$

$$\mathbf{T_{10,9}}=\mathrm{diag}\left(\left.\begin{array}{c|c}1 & \mathbf{0}\\ \hline \mathbf{0} & \mathrm{diag}\left(\left(\frac{R_5}{R_4}\right)^{\omega_n}\right)_n\end{array}\right)_i$$

$$\mathbf{T_{10,10}}=\mathrm{diag}\left(\left.\begin{array}{c|c}\ln R_5 & \mathbf{0}\\ \hline \mathbf{0} & \mathrm{diag}(1)_N\end{array}\right)_i$$

$$\mathbf{T_{10,11}}=\mathrm{diag}\left(\left.\begin{array}{c|c}-1 & \mathbf{0}\\ \hline \mathbf{0} & \mathrm{diag}\left(-\left(1+\left(\frac{R_6}{R_5}\right)^{\omega_n+1}\right)\right)_n\end{array}\right)_i$$

$$\mathbf{T_{11,9}}=\mathrm{diag}\left(\left.\begin{array}{c|c}0 & \mathbf{0}\\ \hline \mathbf{0} & \mathrm{diag}\left(\frac{\omega_n}{R_5}\left(\frac{R_5}{R_4}\right)^{\omega_n}\right)_n\end{array}\right)_i$$

$$\mathbf{T_{11,10}}=\mathrm{diag}\left(\left.\begin{array}{c|c}\frac{1}{R_5} & \mathbf{0}\\ \hline \mathbf{0} & \mathrm{diag}\left(-\frac{\omega_n}{R_5}\right)_n\end{array}\right)_i$$

$$\mathbf{T_{11,11}}=\mathrm{diag}\left(\left.\begin{array}{c|c}0 & \mathbf{0}\\ \hline \mathbf{0} & \mathrm{diag}\left(\frac{\omega_n}{R_5}\left(1-\left(\frac{R_6}{R_5}\right)^{\omega_n+1}\right)\right)_n\end{array}\right)_i$$

$$\mathbf{Y_{10}}=\mathrm{diag}\left(\left.\begin{array}{c}\frac{1}{2}\mu_0 J_{Li}R_6^2\ln R_5+\frac{1}{4}\mu_0\left(J_{Ui}-J_{Li}\right)R_5^2\\ \hline \mathbf{0}\end{array}\right)_i$$

$$\mathbf{Y_{11}}=\mathrm{diag}\left(\left.\begin{array}{c}\frac{1}{2}\mu_0\left(J_{Ui}-J_{Li}+J_{Li}\left(\frac{R_6}{R_5}\right)^2\right)R_5\\ \hline \mathbf{0}\end{array}\right)_i$$

The final assembled equation is shown in (83) at the bottom of the page. The harmonic coefficients of all five subdomains can be obtained by solving the linear equation.

$$\begin{bmatrix} T_{11} & 0 & T_{13} & T_{14} & 0 & 0 & 0 & 0 & 0 & 0 & 0 \\ 0 & T_{22} & 0 & 0 & T_{25} & T_{26} & 0 & 0 & 0 & 0 & 0 \\ T_{31} & 0 & T_{33} & T_{34} & 0 & 0 & 0 & 0 & 0 & 0 & 0 \\ 0 & T_{42} & 0 & 0 & T_{45} & T_{46} & 0 & 0 & 0 & 0 & 0 \\ 0 & 0 & T_{53} & T_{54} & T_{55} & T_{56} & T_{57} & T_{58} & 0 & 0 & 0 \\ 0 & 0 & T_{63} & T_{64} & 0 & 0 & T_{67} & T_{68} & 0 & 0 & 0 \\ 0 & 0 & 0 & 0 & T_{75} & T_{76} & T_{77} & T_{78} & 0 & 0 & 0 \\ 0 & 0 & 0 & 0 & 0 & 0 & T_{87} & T_{88} & T_{89} & T_{8,10} & 0 \\ 0 & 0 & 0 & 0 & 0 & 0 & T_{97} & T_{98} & T_{99} & T_{9,10} & 0 \\ 0 & 0 & 0 & 0 & 0 & 0 & 0 & 0 & T_{10,9} & T_{10,10} & T_{10,11} \\ 0 & 0 & 0 & 0 & 0 & 0 & 0 & 0 & T_{11,9} & T_{11,10} & T_{11,11} \end{bmatrix} \begin{bmatrix} A_I \\ C_I \\ A_{II} \\ B_{II} \\ C_{II} \\ D_{II} \\ A_{III} \\ B_{III} \\ A_{IV} \\ B_{IV} \\ A_V \end{bmatrix} = \begin{bmatrix} Y_1 \\ Y_2 \\ Y_3 \\ Y_4 \\ 0 \\ 0 \\ 0 \\ Y_8 \\ Y_9 \\ Y_{10} \\ Y_{11} \end{bmatrix} \quad (83)$$

REFERENCES

[1] E. Levi, "Multiphase Electric Machines for Variable-Speed Applications," *IEEE Trans. Ind. Electron.,* vol. 55, no. 5, pp. 1893-1909, May 2008.

[2] E. Levi, F. Barrero, and M. J. Duran, "Multiphase machines and drives - Revisited," *IEEE Trans. Ind. Electron.,* vol. 63, no. 1, pp. 429-432, Jan 2016.

[3] M. Barcaro, N. Bianchi, and F. Magnussen, "Faulty Operations of a PM Fractional-Slot Machine With a Dual Three-Phase Winding," *IEEE Trans. Ind. Electron.,* vol. 58, no. 9, pp. 3825-3832, Sep. 2011.

[4] H. S. Che and W. P. Hew, "Dual three-phase operation of single neutral symmetrical six-phase machine for improved performance," in *IECON 2015 - 41st Annual Conference of the IEEE Industrial Electronics Society*, 2015, pp. 001176-001181.

[5] W. N. W. A. Munim, M. J. Duran, H. S. Che, M. Bermúdez, I. González-Prieto, and N. A. Rahim, "A Unified Analysis of the Fault Tolerance Capability in Six-Phase Induction Motor Drives," *IEEE Trans. Power Electron.,* vol. 32, no. 10, pp. 7824-7836, Oct 2017.

[6] H. M. Eldeeb, A. S. Abdel-Khalik, and C. M. Hackl, "Postfault Full Torque–Speed Exploitation of Dual Three-Phase IPMSM Drives," *IEEE Trans. Ind. Electron.,* vol. 66, no. 9, pp. 6746-6756, Sep. 2019.

[7] M. Jones, S. N. Vukosavic, D. Dujic, and E. Levi, "A Synchronous Current Control Scheme for Multiphase Induction Motor Drives," *IEEE Trans. Energy Convers.,* vol. 24, no. 4, pp. 860-868, Dec 2009.

[8] W. N. W. A. Munim, H. S. Che, and W. P. Hew, "Fault tolerant capability of symmetrical multiphase machines under one open-circuit fault," in *4th IET Clean Energy and Technology Conference (CEAT 2016)*, 2016, pp. 1-6.

[9] Y. Zhou, X. Lin, and M. Cheng, "A Fault-Tolerant Direct Torque Control for Six-Phase Permanent Magnet Synchronous Motor With Arbitrary Two Opened Phases Based on Modified Variables," *IEEE Trans. Energy Convers.,* vol. 31, no. 2, pp. 549-556, June 2016.

[10] H. Lu, J. Li, R. Qu, D. Ye, and Y. Lu, "Fault-Tolerant Predictive Control of Six-Phase PMSM Drives Based on Pulsewidth Modulation," *IEEE Trans. Ind. Electron.,* vol. 66, no. 7, pp. 4992-5003, July 2019.

[11] F. Dubas and C. Espanet, "Analytical solution of the magnetic field in permanent-magnet motors taking into account slotting effect: no-load vector potential and flux density calculation," *IEEE Trans. Magn.,* vol. 45, no. 5, pp. 2097-2109, May 2009.

[12] Z. Q. Zhu, L. J. Wu, and Z. P. Xia, "An accurate subdomain model for magnetic field computation in slotted surface-mounted permanent-magnet machines," *IEEE Trans. Magn.,* vol. 46, no. 4, pp. 1100-1115, April 2010.

[13] L. J. Wu, Z. Q. Zhu, D. Staton, M. Popescu, and D. Hawkins, "An improved subdomain model for predicting magnetic field of surface-mounted permanent magnet machines accounting for tooth-tips," *IEEE Trans. Magn.,* vol. 47, no. 6, pp. 1693-1704, June 2011.

[14] M. Markovic, M. Jufer, and Y. Perriard, "Reducing the cogging torque in brushless DC motors by using conformal mappings," *IEEE Trans. Magn.,* vol. 40, no. 2, pp. 451-455, March 2004.

[15] K. Boughrara, R. Ibtiouen, D. Zarko, O. Touhami, and A. Rezzoug, "Magnetic Field Analysis of External Rotor Permanent-Magnet Synchronous Motors Using Conformal Mapping," *IEEE Trans. Magn.,* vol. 46, no. 9, pp. 3684-3693, Sep. 2010.

[16] D. Zarko, D. Ban, and T. A. Lipo, "Analytical calculation of magnetic field distribution in the slotted air gap of a surface permanent-magnet motor using complex relative air-gap permeance," *IEEE Trans. Magn.,* vol. 42, no. 7, pp. 1828-1837, July 2006.

[17] L. J. Wu, Z. Q. Zhu, D. Staton, M. Popescu, and D. Hawkins, "Subdomain model for predicting armature reaction field of surface-mounted permanent-magnet machines accounting for tooth-tips," *IEEE Trans. Magn.,* vol. 47, no. 4, pp. 812-822, April 2011.

[18] A. Rahideh and T. Korakianitis, "Analytical Magnetic Field Calculation of Slotted Brushless Permanent-Magnet Machines With Surface Inset Magnets," *IEEE Trans. Magn.,* vol. 48, no. 10, pp. 2633-2649, Oct 2012.

[19] T. Lubin, S. Mezani, and A. Rezzoug, "Two-Dimensional Analytical Calculation of Magnetic Field and Electromagnetic Torque for Surface-Inset Permanent-Magnet Motors," *IEEE Trans. Magn.,* vol. 48, no. 6, pp. 2080-2091, June 2012.

[20] K. Boughrara, R. Ibtiouen, and T. Lubin, "Analytical Prediction of Magnetic Field in Parallel Double Excitation and Spoke-Type Permanent-Magnet Machines Accounting for Tooth-Tips and Shape of Polar Pieces," *IEEE Trans. Magn.,* vol. 48, no. 7, pp. 2121-2137, July 2012.

[21] Z. Q. Zhu, D. Howe, and C. C. Chan, "Improved analytical model for predicting the magnetic field distribution in brushless permanent-magnet machines," *IEEE Trans. Magn.,* vol. 38, no. 1, pp. 229-238, Jan 2002.

[22] Z. Q. Zhu, D. Ishak, D. Howe, and J. Chen, "Unbalanced Magnetic Forces in Permanent-Magnet Brushless Machines With Diametrically Asymmetric Phase Windings," *IEEE Trans. Ind. Appl.,* vol. 43, no. 6, pp. 1544-1553, Nov 2007.

Zhe Liang (Member, IEEE) received his B.S. degree in electrical engineering from Xi'an Jiaotong University, Xi'an, China, in 2012. From the same university, he received his Ph.D. degrees in electrical engineering in 2021.

Currently he is a postdoctoral associate researcher at the School of Energy and Power Engineering, Xi'an Jiaotong University, Xi'an, China. His research interests include motion control, fault tolerant control, multiphase permanent magnet motor, and all-electric aircraft.

Deliang Liang (Senior Member, IEEE) received the BS, MS and PhD degrees in Electrical Engineering from Xi'an Jiaotong University, Shaanxi, China in 1989, 1992 and 1996, respectively.

Since 1999, he has been with the School of Electrical Engineering, Xi'an Jiaotong University, where he is currently a professor. From 2001 to 2002, he was a visiting scholar with Science Solution International Lab., Tokyo, Japan. His research fields include optimal design, control, and simulation of electrical machines.

Peng Kou (Senior Member, IEEE) received his B.S. degree in electrical engineering from Xi'an Jiaotong University, China, in 2005. From the same university, he received his M.S. and Ph.D. degrees in control science and engineering in 2008 and 2013, respectively. From 2015 to 2016, he was a visiting scholar at The Ohio State University, Columbus, USA.

Currently he is an associate professor at the School of Electrical Engineering, Xi'an Jiaotong University. His research interests include model predictive control, motor control, and all-electric aircraft.

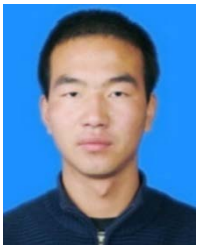

ShaoFeng Jia (Member, IEEE) was born in Shaanxi, China. He received the B.Eng. degree in electrical engineering from Xi'an Jiaotong University, Xi'an, China, in 2012, and Ph.D. degree in electrical engineering from the Huazhong University of Science and Technology, Wuhan, China, in 2017.

He is currently an Associate Professor with the School of Electrical Engineering, Xi'an Jiaotong University. He is the Author/Co-Author of about 70 IEEE technical papers. His research interests include design and control of novel PM and reluctance machines.